Downstream Semi-Circular Obstacles' Influence on Floods Arising from the Failure of Dams with Different Levels of Reservoir Silting

Foad Vosoughi [a], Mohammad Reza Nikoo [b *], Gholamreza Rakhshandehroo [c], Jan Franklin Adamowski [d], and Amir H. Gandomi [e]

[a] Research Associate, Department of Civil and Environmental Engineering, Shiraz University, Shiraz, Iran. Email: foad.vosooghi@gmail.com

[b] (Corresponding Author), Associate professor, Department of Civil and Architectural Engineering, Sultan Qaboos University, Muscat, Oman. Email: m.reza@squ.edu.om

[c] Professor, Department of Civil and Environmental Engineering, Shiraz University, Shiraz, Iran. Email: rakhshan@shirazu.ac.ir

[d] Professor, Department of Bioresource Engineering, McGill University, 21111 Lakeshore Road, Saint-Anne-de-Bellevue, QC, Canada. Email: jan.adamowski@mcgill.ca

[e] Professor, Faculty of Engineering and Information Technology, University of Technology Sydney, Ultimo, NSW 2007, Australia. Email: gandomi@uts.edu.au

** Corresponding author; Email: m.reza@squ.edu.om*

ABSTRACT

Dam-break wave-propagation in a debris flood event is strongly influenced by accumulated reservoir-bound sediment and downstream obstacles. For instance, the Brumadinho dam disaster in January 2019 released 12×10^6 m^3 of mud and iron tailings and inflicted 270 casualties. The present work was motivated by the apparent lack of experimental or numerical studies on silted-up reservoir dam-breaks with downriver semi-circular obstacles. Accordingly, 24 dam-break scenarios with different reservoir sediment depths and with or without obstacles were observed experimentally and verified numerically. Multiphase flood waves were filmed, and sediment depths, water levels and values of front wave celerity were measured to improve our scientific understanding of shock wave propagation over an abruptly changing topography. The strength of OpenFOAM software in estimating such complex phenomenon was assessed using two approaches: Volume of Fluid (VOF) and Eulerian. An acceptable agreement was attained between numerical and experimental records (errors ranged from 1 to 13.6%), with the Eulerian outperforming the VOF method in estimating both sediment depth and water level profiles. This difference was most notable when more than half of the reservoir depth was initially filled by sediment (≥ 0.15 m) and particularly in bumpy bed scenarios.

Keywords: Silted-Up Dam-break, Semi-Circular Obstacle, Image Processing, Abruptly Changing Topography, Multiphase Shock Wave, OpenFOAM

INTRODUCTION

Sediment deposition in dam-bound reservoirs has become a considerable and widely occurring problem, posing a serious challenge to the design of and completion of dams (Vischer and Hager 1998). The problem is particularly critical for smaller reservoirs lacking a bottom outlet system, as these frequently become completely silted-up (Vischer and Hager 1998). Floods, which involve the mixing of a massive saturated sediment layer with free surface water, occur predominantly during dam-break events that are coupled with silted-up reservoirs (Shi et al. 2019). Considering the complex phenomena generated by such events, the behaviour of three phases must be considered: air, clear water (no sediment), subtended by a saturated sediment level (Duarte et al. 2011).

A break in a silted-up dam results in the movement of dense sediment deposited in the reservoir and may lead to irreparable destruction and casualties. Infrastructure and agricultural areas located along the dam, downstream of the dam, or in the lower reaches of adjacent river basins may be buried under a large quantity of mud and debris flow. For instance, in January 2019, Brazil's Brumadinho dam-break released roughly 12×10^6 m^3 of iron ore tailings and mudflow, which destroyed houses, farms, inns, mine's offices, and roads downstream from the dam. In the Brumadinho township, many agricultural areas were affected or totally destroyed, and at least 270 people died (Wikipedia 2019).

Interactions between reservoir water and the large volume of sediment stored in dam reservoirs strongly affect sediment layer motion and flood propagation (Yang 1996). In addition, structures and installations located in flood-prone areas downstream from a dam may act as obstacles to a flood's propagation following a dam-break, with potentially harmful consequences in terms of the collapse of remaining structures. The presence of such obstacles in the flood plain adjoining the river may also influence flood characteristics, such as wave velocity and depths downstream from obstacles. Consequently, the accurate prediction of silted-up dam-break flow behaviour over natural terrain and bumpy downstream reaches is vital to prevent and mitigate catastrophic flood disasters.

Although the failure of dams retaining water-filled reservoirs (no sediment) is a major consideration in hydraulic engineering and has been widely scrutinised numerically and experimentally, only a few studies have investigated the severe problems of sedimentation in dam reservoirs (Duarte et al. 2011).

Most relevant experimental (Xue et al. 2011) and numerical studies (Wu and Wang 2007; Valiani et al. 2002) on reservoirs with sedimentation were only recently conducted in the 21st century. The characteristics of dam-breaks and their resulting flood waves were extensively investigated and documented for clear water, with experiments addressing a wide range of upstream and downstream initial simple conditions but only simple one- or two-dimensional scenarios (Wu and Wang 2007; Valiani et al. 2002). While past studies mostly focused on constant bed scenarios (Crespo et al. 2008), the role of sediment movement in failure of a dam with a mobile bed has lately gained more attention (Postacchini et al. 2014; Evangelista et al. 2013). To the best of the authors' knowledge, there are limited numerical or experimental studies concerning dam-break multiphase shock flood waves from a reservoir with a high degree of silting.

Recently, the incorporation of downstream obstacles into increasingly complex mobile-bed dam-break scenarios has been studied (Issakhov and Imanberdiyeva 2019; Kattel et al. 2018; Kamra et al. 2019; Mokhtar et al. 2019). Specifically, these works used considered obstacles of various geometric shapes, such as a vertical wall (Mokhtar et al. 2019), triangular-shaped barriers (Ozmen-Cagatay et al. 2014), lateral sidewalls (Kocaman et al. 2012), vertical cylinder (Kamra et al. 2019), single cube (Aureli et al. 2015), and group of cubes (Goseberg et al. 2016; Güney et al. 2014). Moreover, there have been extensive numerical studies on the influence of obstacles on dam-break phenomena (Gallegos et al. 2009; Hänsch et al. 2014; Jeong et al. 2012; Saghi and Lakzian 2019; Singh et al. 2011). A dam-break is usually investigated numerically with triangular downstream obstacles (Kattel et al. 2018; Cheng et al. 2017; Saghi and Lakzian 2019; Singh et al. 2011) or a group of cubes to represent an urban area (Jeong et al. 2012; Wang et al. 2017). However, similar scenarios with a vertical wall (Hänsch et al. 2014), single cube (Aureli et al. 2015), trapezoidal obstacles (Issakhov et al. 2018; Kattel et al. 2018), and groups of obstacles that represent vegetation have also been studied numerically (He et al. 2017). Since typical forms of obstacles in nature are semi-circular (e.g., humps and hill-like barriers), rounded downstream obstacles with different cross-sections were investigated in the present study to better reflect natural terrain. To the authors' knowledge, such obstacles have rarely been presented in the literature compared to triangular and trapezoidal obstacles.

Shock floods arising from dam-break phenomena on a mobile bed and sediment motion in open channel flows are critical issues and have been investigated both numerically and experimentally (Shi et al. 2019; Fu and Jin 2016; Zhang and Wu 2011; Mambretti et al. 2008). Nevertheless, there is a great distinction between the usual sediment height in a typical reservoir or river bed and the high sediment level in a silted-up reservoir, which has rarely been addressed (Duarte et al. 2011).

A rigorous literature review revealed the limited amount of studies on the behaviour of floodwaters when they meet a semi-circular obstacle in situations where the failed dam had a silted-up reservoir. Therefore, our study is novel in that it involved both experimental analysis and numerical verification of multi-layer shock wave characteristics (e.g., water level, sediment depth, and wave celerity) in a situation where semi-circular obstacles were present. Various upstream sediment depths, which occupied 10-80% of the reservoir's total height, combined with the downstream presence or absence of semi-circular obstacles of various cross-sections at a specified distance from a dam section, created 24 different scenarios. The experimental results were carefully filmed using high-speed professional cameras. Experimental data, including water levels and sediment depths along the experimental flume, have been provided and can be used for validation in other studies. The numerical portion of the current research verified the 24 dam-break experimental scenarios via OpenFOAM software using two distinct methods (Open∇FOAM 2015): VOF (Volume of Fluid) and Eulerian. Laboratory records were rigorously compared with the predictions of both numerical methods.

EXPERIMENTAL MODELLING

All experiments were performed in the Hydraulic Lab of Shiraz University (Iran). The dimensions of the studied rectangular channel were 0.3 m width, 6 m length, and 0.32 m depth, including a horizontal smooth bed. The bottom was steel, and both lateral walls were glass. The length of the flume was partitioned via a moving gate installed to create a reservoir with a length of 1.52 m (Fig. 1a), and a downstream channel with a length of 4.5 m (Vosoughi 2018). Dam-break waves were produced in the downstream part of the flume by the instantaneous release of reservoir water. The effects of semi-circular downstream obstacles on multiphase flood waves in an initially dry-bed downstream were examined. The schematic illustration of the three-phase shock wave propagating along the flume and over the hump is detailed in Fig. 1b. Representing natural topography, the hump can lead to a sudden change in flood wave propagation in certain parts of the downstream channel.

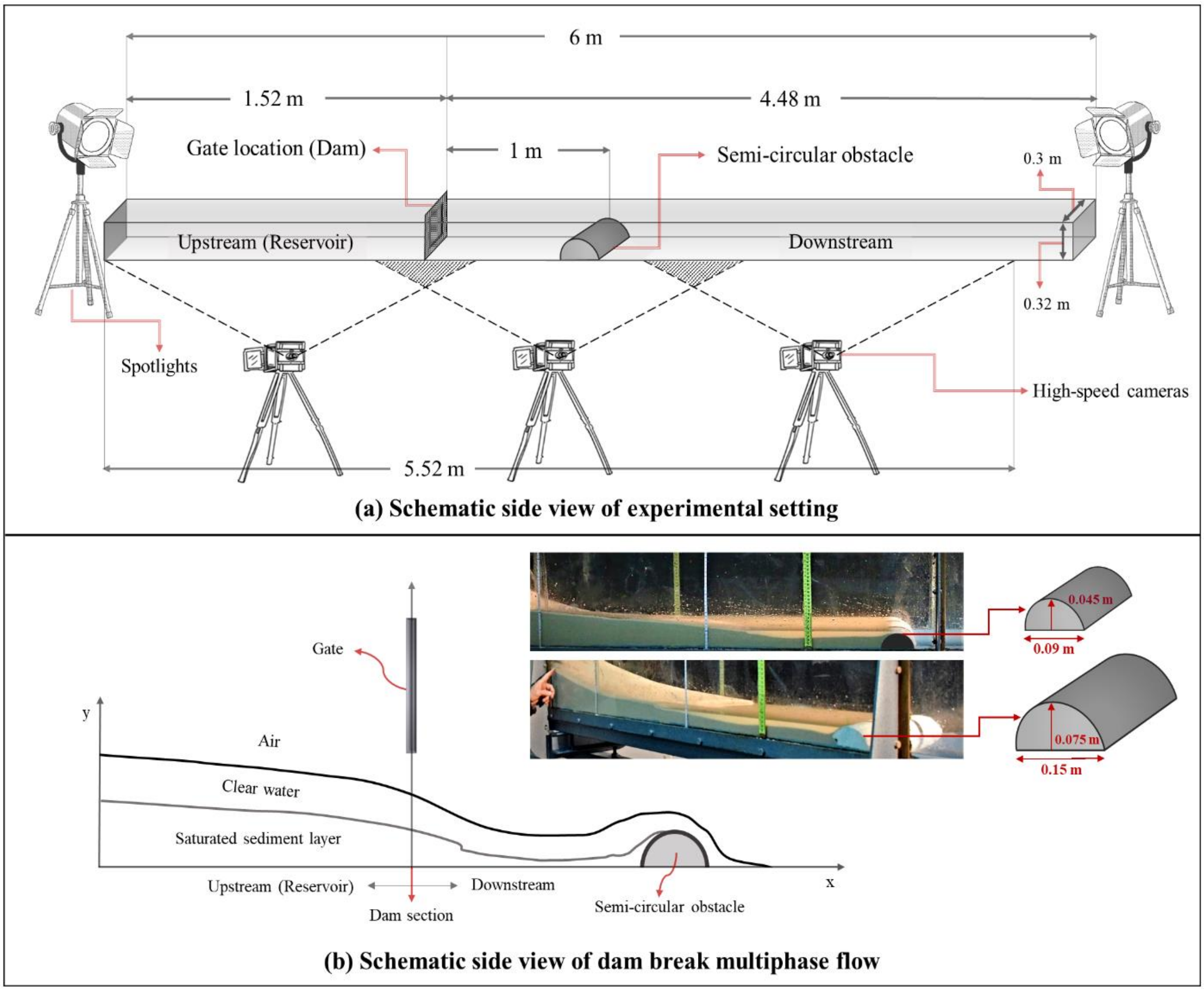

Fig. 1. Schematic side view of (a) experimental setting (b) dam break multiphase flow. a) Plan view of flume components, instruments' locations and the obstacle position. All not to scale (Vosoughi 2018). b) Side view of silted-up dam break wave propagation over a downstream semi-circular obstacle and the schematic geometry of obstacles

Experimental set-up

The experimental environment, facilities, and instruments used in this study are shown in Figures 2a-g. Throughout the 6-month study, three high-speed cameras were mounted in fixed positions at equal intervals over the 5.52 m stretch of the flume (Figs. 2c-e) to record videos and collect high-quality water level, sediment depth. Two powerful spotlights were located at each channel extremity to provide illumination. The flume was equipped with a sudden opening gate (i.e., the dam) and a position to affix the semi-circular obstacle downstream from the dam (Fig. 1). The gate consisted of two plates made of Plexiglass separated by a wider rubber layer (to prevent leakage at the edges) and totalled 0.01 m in thickness. Two powerful wooden clamps were attached to the gate to make it more stable. Grease was applied to the edges of the gate to allow for easier motion. The beginning of the reservoir was blocked by two walls fabricated with Styrofoam sheets and medium-density fibreboard (MDF).

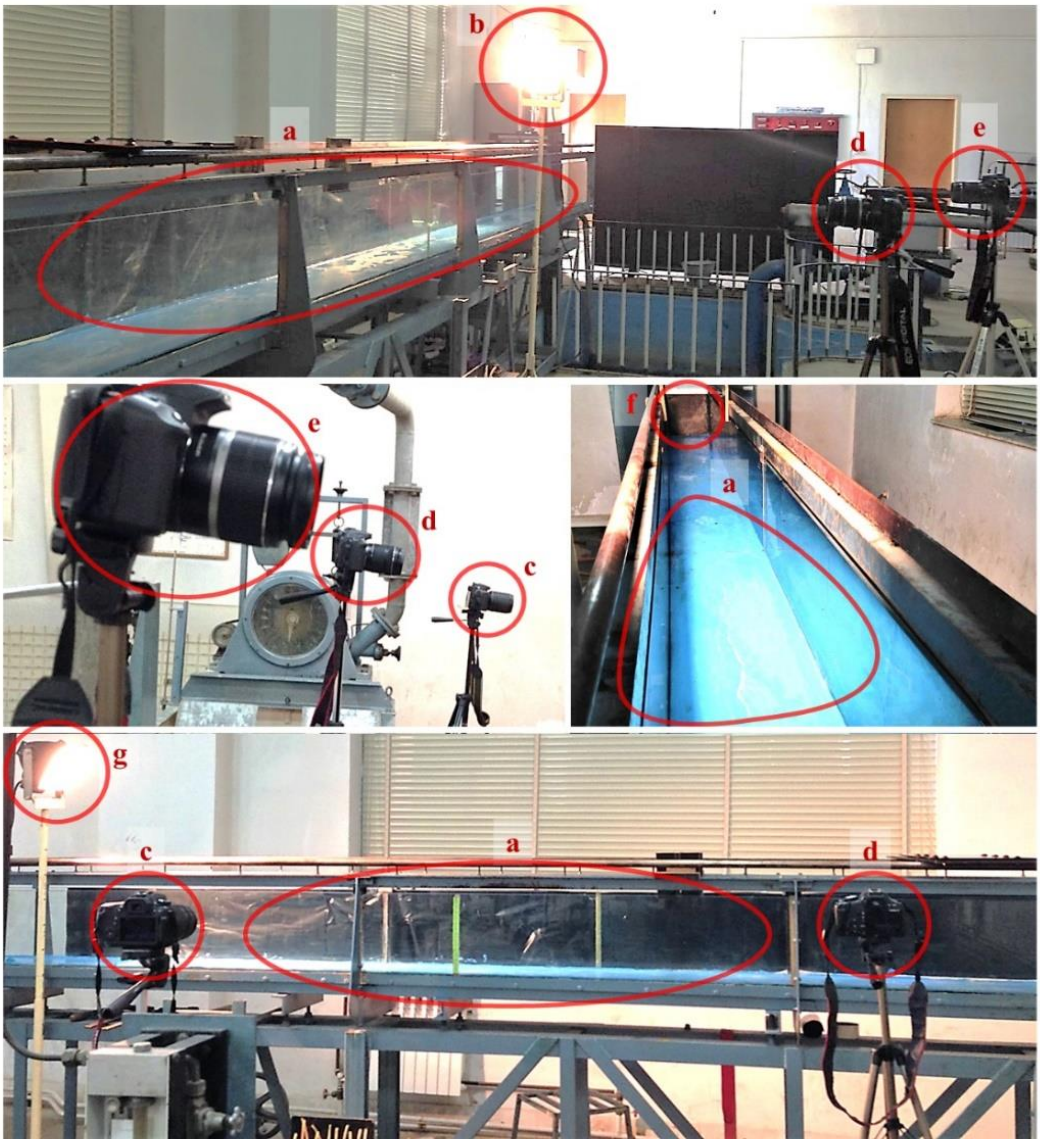

Fig. 2. Experimental environment and facilities; (a) highly exposed zone inside the flume, (b & g) right and left spotlights, respectively, (c, d & e) first, middle and third cameras, respectively, (f) onset of the reservoir (channel's first point)

In order to simulate a silted-up reservoir, a quartz sand mixture with uniform grain sizes of mainly 0.2-0.4 mm in diameter (see Supplementary Material; Table S1 and Fig. S1) served as the experimental dam-retained sediment. Prior to each test, the sediment was rinsed and desiccated, the reservoir was filled to the required sediment depth, and the horizontal surface of the sediment layer was smoothed by hand with a putty knife. Water was then injected at a very low rate into the reservoir up to a height

(h_0) of 0.3 m. After each test, the flume was cleaned and dried in order to keep adhesive forces between the flume and other materials relatively constant.

To physically simulate dam-break flow, a complex mechanism was constructed and installed in the flume with a gate (dam) that could be suddenly lifted. The sluice gate release time should be smaller than $\sqrt{2\,(h_0/g)}$, where g represents the acceleration of gravity (Lauber and Hager 1998). Considering $h_0 = 0.3$ m, the greatest release time was calculated as 0.247 s. However, the actual sluice gate release time ranged from 0.08 to 0.16 s, which was confirmed using high-speed videos.

Experimental scenarios

A reservoir with clear water (no sediment) and seven distinct depths of sediment (S_0= 0.03, 0.075, 0.15, 0.175, 0.2, 0.22, and 0.24 m) were tested as the initial conditions in the upstream to scrutinize different silted-up flood depths and velocities. A completely dry bottom with or without an obstacle was set as the downstream hydraulic conditions. Scenarios in the absence of downstream obstacles (smooth bed) were considered to obtain an appropriate comparison basis for other initial conditions.

Two humps (semi-circular obstacles) with various cross-sections (0.045 and 0.075 m) were firmly installed at the bottom of the downstream channel (1 m after the dam section) and further stuck to the channel's side walls using rubber sheets. Both obstacles were made of Styrofoam sheets with a schematic geometry, as illustrated in Fig. 1b; the obstacles displayed lengths of 0.3 m and widths of 0.09 and 0.15 m. A relatively heavy weight was bolted to the obstacle's downstream side to provide sufficient stability during flood wave impacts. The obstacles' O_r/h_0 ratios were 0.15 and 0.25, where h_0 and O_r represents the initial reservoir water level and downstream obstacle's radius, respectively. Table 1 lists the 24 scenarios examined in this research, outlining the upstream sediment depths and downstream hydraulic conditions. To verify repeatability, achieve high quality data, and ensure reliable results, scenarios were repeated twice. Changes between experimental replicates remained under 3%.

Data collection and image processing

A digital image processing technique was applied to measure the required physical parameters from silted-up dam-break shock waves over a bumpy downstream bed. The high-quality data were acquired by simultaneous imaging with three high-speed digital cameras (Canon EOS 70D) that covered the entire channel length and operated at fifty frames per second. All raw recorded videos had a resolution of 1920×1080 pixels (Full HD/1080p). To create sufficient contrast for filming and avoid uncontrolled lights and reflections, the surrounding laboratory was partly isolated using black curtains installed behind the cameras. Windows were covered with thick dark plastic sheets, and a black curtain was installed on opposite side of the flume's wall to mask objects behind it. Three video files were obtained from the cameras after each experiment and transferred to the computer. Required parameters, including water levels and sediment depths, were extracted by analysing the first 300 frames (6 s @ 50 fps).

Table 1. List of the experimental scenarios investigated in the present study

# Scenarios	S_0 (m)	$\frac{S_0}{h_0}$ (%)	O_r (m)	$\frac{O_r}{h_0}$ (%)	# Scenarios	S_0 (m)	$\frac{S_0}{h_0}$ (%)	O_r (m)	$\frac{O_r}{h_0}$ (%)
1	Clear water	0	No obstacle	0	**13**	0.0175	58.3	No obstacle	0
2	Clear water	0	0.045	15	**14**	0.0175	58.3	0.045	15
3	Clear water	0	0.075	25	**15**	0.0175	58.3	0.075	25
4	0.03	10	No obstacle	0	**16**	0.2	66.7	No obstacle	0
5	0.03	10	0.045	15	**17**	0.2	66.7	0.045	15
6	0.03	10	0.075	25	**18**	0.2	66.7	0.075	25
7	0.075	25	No obstacle	0	**19**	0.22	73.3	No obstacle	0
8	0.075	25	0.045	15	**20**	0.22	73.3	0.045	15
9	0.075	25	0.075	25	**21**	0.22	73.3	0.075	25
10	0.15	50	No obstacle	0	**22**	0.24	80	No obstacle	0
11	0.15	50	0.045	15	**23**	0.24	80	0.045	15
12	0.15	50	0.075	25	**24**	0.24	80	0.075	25

Note: S_0 = Initial upstream sediment depth (m); O_r = Obstacle radius (m).

More than 10 measuring rulers with an accuracy of ±1 mm were mounted vertically on the sides of the flume, roughly 0.50 m apart along its length, and used to measure water levels and sediment depths at any arbitrary point along the flume. Several rulers monitored by two adjacent cameras were employed as references to align the extracted photographs. Two striped rulers, each with an accuracy of ±1 mm, were pasted horizontally on the upper and lower portions of the lateral wall. The study evaluated 20 positions along the flume (Fig. 3): 0.00, 0.76, 1.02, 1.27, 1.37, 1.42, 1.47, 1.52, 1.57, 1.67, 1.77, 1.87, 2.42, 2.47, 2.52, 2.57, 2.62, 3.52, 4.52, and 5.52 m. Fifteen post-dam-break snaps were assessed: 0.04, 0.08, 0.12, 0.2, 0.3, 0.4, 0.6, 0.8, 1, 1.5, 2, 3, 4, 5, and 6 s. A total of 1080 video images (24 different scenarios, 15 snap times and 3 cameras) were rigorously analysed. Image editing was required to obtain adequate contrast and minimize interfering lights and reflections. Consequently, the sharpness, brightness, contrast, and colour of the photos were adjusted to better identify the interfaces between air, water, and sediment layers. This procedure was repeated for all images.

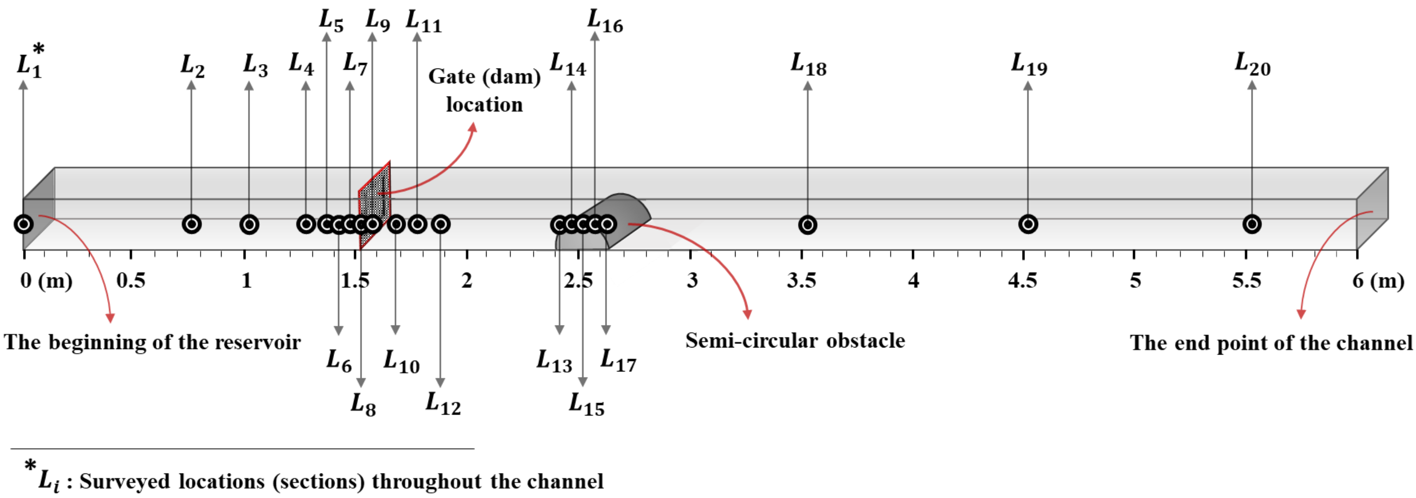

Fig. 3. A graphic picture of the experimental channel; L1 to L20 are depth gauging locations

A non-disturbing procedure was consecutively employed for each video image via Grapher®. After initiating the coordinates of at least two confirmed positions in each photograph on a diagonal line, clicking on any random spot would lead to a presentation of the coordinates of that spot on the *x*- and *y*-axes. Hence, the development of water and sediment depths with time (*h* versus *t*) could be acquired precisely from photographs for any arbitrary chosen spot, without any flow interruptions resulted from experimental devices. The sediment depth and water level profiles along the flume could thus be obtained at any time after the dam-break. Although this procedure was laborious, it led to high-quality and precise outcomes. Since two physical parameters were extracted from 20 locations along the flume, all images comprised 14400 data points (2 parameters × 20 locations × 15 times × 24 scenarios); these are available online in the public repository accompanying this study (Vosoughi et al. 2021a; b; c). The practical purpose of performing this process was to accurately investigate the areas buried by the sediment layer at specific times and snapshots (time-steps) after the dam-break.

To validate the experimental modelling records, a specific dam-break scenario was modelled both numerically and experimentally for various initial downstream bed conditions, including dry- and wet-beds (Vosoughi 2018). Outcomes were evaluated by comparison with results of previously published reports (Fig. 4) (Ozmen-Cagatay and Kocaman 2010). Fig. S2 in the Supplementary Material compares the experimental records quantitatively with experimental measurements from the literature (LaRocque et al. 2013). A set of experimental video images at 12 snap times after the failure of the dam (from 0 to 40 s) when the initial sediment depth in the reservoir was 0.22 m and a 0.075-m-tall obstacle was mounted on the downstream channel bottom is presented in the Supplementary Material (Fig. S5).

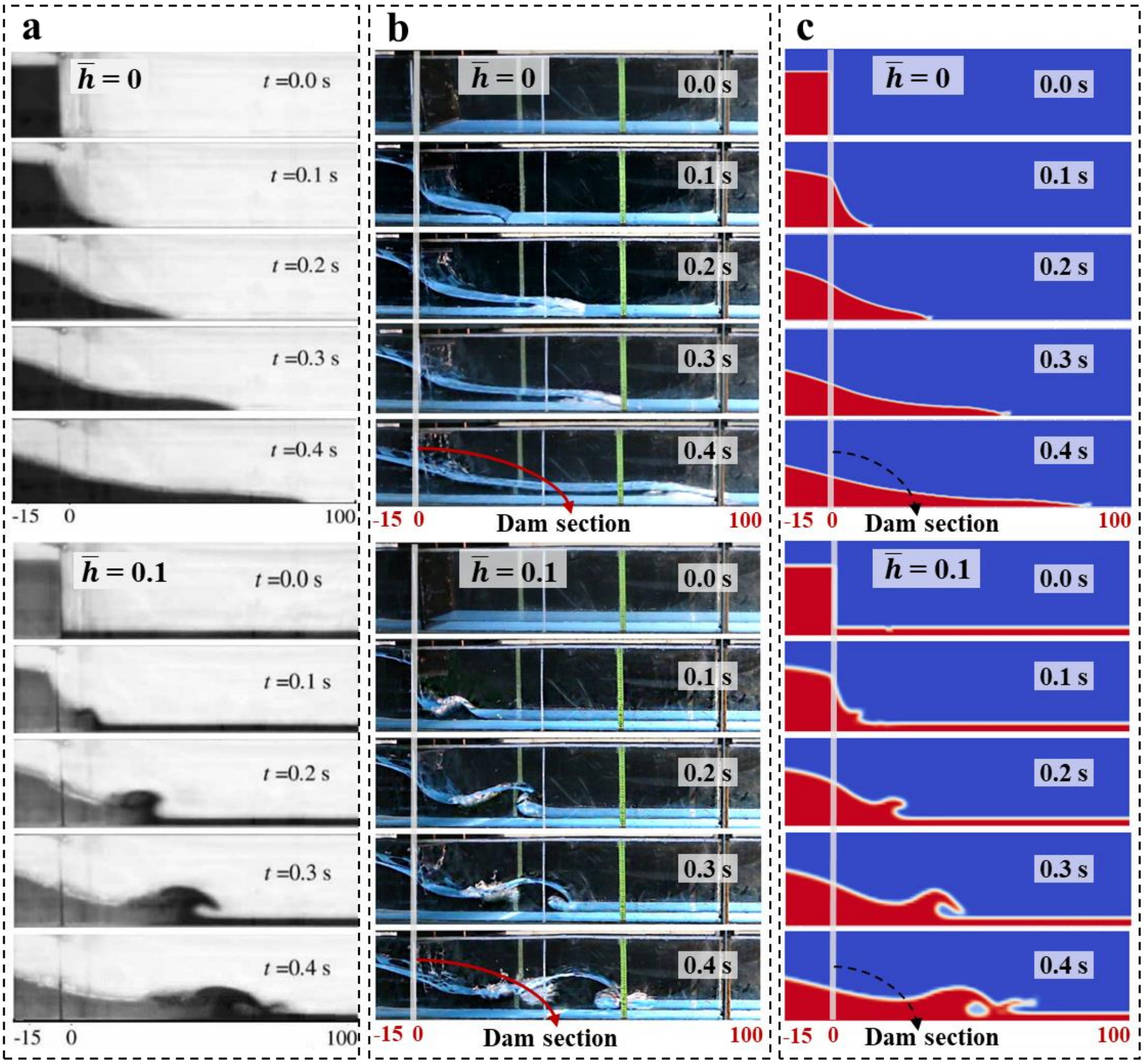

Fig. 4. Image-based comparison of dam-break shock waves side views *h(x)* at various time snaps: (a) available laboratory records (Ozmen-Cagatay and Kocaman 2010), (b) current laboratory records (Vosoughi 2018), and (c) OpenFOAM results (Vosoughi 2018). Unit of length is cm, and $\bar{h}$ is the ratio of downstream initial water depth to initial upstream height of 0.3 m

NUMERICAL MODELLING

In the numerical modelling portion of the study, an open-source and license-free CFD (computational fluid dynamics) package called OpenFOAM was employed (Open∇FOAM 2015). This software is the best-known and most frequently used free CFD package, which operates on the Linux kernel operating system. Its source code is easily expandable as it employs the object-oriented programming language, C^{++} (Openfoamwiki 2020). As previously mentioned, numerical modelling concerning the effect of semi-circular obstacles on the multi-layer waves arising from a silted-up dam-break has not been performed to-date. For the presented study, the purpose of performing this numerical process was to verify the relative responsiveness of simple numerical models, which are also publicly available, to predict this complex phenomenon and experimental data.

Euler-Euler approach

The Euler-Euler approach is a dominant numerical method in OpenFOAM to model multi-layer flows, in which each phase is mathematically treated as a continuum. Thus, these models are called "multi-fluid models", which can appropriately demonstrate separated flows where each phase may be categorized as a continuum. The Euler-Euler method may also be utilized to model discrete flows, where the full movement of phases is of interest rather than exploring a single phase. This approach is particularly helpful when detecting the boundary between phases is preferred (Nilsson 2010). In order to specify a discrete phase as a continuum, the particles' volume fraction must be high; therefore, this method is appropriate for modelling condensed flow. Additionally, since particles are spread and, yet, defined as a continuous layer, conservation equations may be employed to model such layers (Open∇FOAM 2015).

Once a silted-up flood propagates, the saturated sediment deposit might act similarly to a viscid fluid until it stops completely and the water layer flows smoothly over its top (Duarte et al. 2011). In this study, the saturated sediment phase was assumed to be a highly viscid fluid. The three Euler-Euler multiphase models in OpenFOAM (Open∇FOAM 2015) included the volume of fluid (VOF), Eulerian, and mixture models. The wave following the failure of a silted-up dam and how it propagates over downstream semi-circular obstacles was simulated using VOF and Eulerian models. It is pertinent to mention that these models were applied in this study as it was assumed that all phases were continuous.

Volume of fluid (VOF) model

The volume of fluid (VOF) model is a subset of the Euler-Euler approach, where each phase is treated as a continuum. Although interpenetrating of the layers is not allowed, the purpose of this method is to model non-miscible (layered) multi-fluids particularly when the interface position among the fluids is significant. This method considers a particular group of equations of continuity and momentum, which are resolved and shared for each flow layer, whilst the fluid volume fraction is tracked in each of the cells within the computational domain. The VOF model can address a wide spectrum of issues, such as free surface flows and dam-break waves. In this study, VOF simulations were ran using the *interFoam,* and *multiphaseInterFoam* solvers.

In the VOF model, the properties used in the governing equations are defined for all phases in each of the control volumes. For instance, in a dual-phase model, if the second phase's volume fraction is being tracked, the density, ρ, for each of the cells is presented by (Torres et al. 2021):

$$\rho = \alpha_2 \rho_2 + (1 - \alpha_2)\rho_1 \tag{1}$$

where α_2 is the water fraction; and ρ_1 and ρ_2 are the densities of air and clear water, respectively.

Generally, for a *k*-phase model, the volume-fraction-averaged viscosity, μ_m, and the volume-fraction-averaged density, ρ_m, take on the following forms (Barbosa et al. 2019; Wang et al. 2020b):

$$\mu_m = \sum_{i=1}^{k} \mu_i \alpha_i \tag{2}$$

$$\rho_m = \sum_{i=1}^{k} \rho_i \alpha_i \tag{3}$$

Then, the apparent viscosity, μ_m, and density, ρ_m, of multiphase silted-up flood waves are calculated as $\mu_m = \mu_1\alpha_1 + \mu_2\alpha_2 + \mu_3\alpha_3$ and $\rho_m = \rho_1\alpha_1 + \rho_2\alpha_2 + \rho_3\alpha_3$, in which, μ_1, μ_2 and μ_3 are the viscosities and ρ_1, ρ_2 and ρ_3 are the densities of air, clear water, and saturated sediment layer, respectively. Each phase fraction, α_k, is also defined in relation to the other phase fractions, whereby the sum of all volume fractions should be equal to 1 (Wang et al. 2020b):

$$\sum_{i=1}^{k} \alpha_i = 1 \tag{4}$$

In this study, the air fraction, α_1 is defined in relation to the water fraction, α_2, and saturated sediment layer fraction, α_3, while $\alpha_1 + \alpha_2 + \alpha_3 = 1$.

The three-phase flood wave equations solved in the VOF method for isothermal and incompressible flow are presented below as a group equation of continuity and momentum (Barbosa et al. 2019; Miliani et al. 2021; Panda et al. 2017; Torres et al. 2021; Wang et al. 2020a; b):

$$\frac{\partial \rho_m}{\partial t} + \nabla \cdot (\rho_m \mathbf{U}) = 0 \tag{5}$$

$$\frac{\partial \rho_m \mathbf{U}}{\partial t} + \nabla \cdot (\rho_m \mathbf{U}\mathbf{U}) = -\nabla \mathbf{P} + \nabla \cdot \boldsymbol{\tau} + \rho_m \mathbf{g} + \mathbf{S} = 0 \tag{6}$$

where ρ_m represents the volume-fraction-averaged density; $\mathbf{U}$ is the velocity; $\mathbf{g}$ is the “gravitational acceleration”; $\boldsymbol{\tau}$ denotes the “viscous stress tensor”; $\mathbf{P}$ is pressure; and $\mathbf{S}$ is the force due to the “surface tension”. The “viscous stress tensor”, $\boldsymbol{\tau}$, is also described as (Barbosa et al. 2019; Wang et al. 2020b):

$$\boldsymbol{\tau} = \mu_m[(\nabla \mathbf{U}) + (\nabla \mathbf{U})^{\mathrm{T}}] \tag{7}$$

where $\nabla \mathbf{U}$ denotes the gradient of the velocity. In Cartesian coordinates, $\nabla \mathbf{U}$ is the Jacobian matrix, and $(\nabla \mathbf{U})^{\mathrm{T}}$ is the transpose of the gradient $\nabla \mathbf{U}$ (Wang et al. 2020a). In OpenFOAM, there are two surface tension models: the “continuum surface force” (CSF) and “continuum surface stress” (CSS). In the CSF, the nonconservative form of the surface tension force, $\mathbf{S}$, may be described as (Wang et al. 2020b):

$$\mathbf{S} = \sigma K \nabla \alpha \tag{8}$$

where σ is the “surface tension constant”; α represents the volume fraction of the fluid; and K is the “curvature of the surface”, given by (Wang et al. 2020b):

$$K = -\nabla \left(\frac{\nabla \alpha_k}{|\nabla \alpha_k|} \right) \tag{9}$$

where $\nabla \alpha = \hat{n}$ is the vector normal to the interface (see Eq. 17); and the surface tension constant, σ, is set to be a constant (0.07 N/m) for all phases (Table 2). Also, considering α_k as a function of time in order to approximate the interphases’ position, the transport equation for α_k must be solved:

$$\frac{\partial \alpha_k}{\partial t} + \nabla \cdot (\alpha_k \mathbf{U}) = 0 \tag{10}$$

OpenFOAM applies the interface capturing technique (Weller 2008) by introducing an additional compressive term in Eq. (10). The extended transport equation for the volume fraction α_k used in *multiphaseInterFoam* solver may be described as:

$$\frac{\partial \alpha_k}{\partial t} + \nabla \cdot (\mathbf{U}\alpha_k) + \nabla \cdot [\mathbf{U}_r \alpha_k (1 - \alpha_k)] = 0 \tag{11}$$

where the relative velocity, $\mathbf{U}_r$, is employed in the interface to compress the "volume fraction" area and keep the interface sharp (Wang et al. 2020b); and $\alpha_k(1 - \alpha_k)$ is a nonzero term that guarantees that the compression term is effective in the interface area. $\mathbf{U}_r$, is also presented by (Barbosa et al. 2019):

$$\mathbf{U}_r = min(C_\alpha |\mathbf{U}|, max(|\mathbf{U}|)) \frac{\nabla \alpha}{|\nabla \alpha|} \tag{12}$$

where the compressibility coefficient, C_α, is applied to control interfacial compression. The min operator is locally operated on each cell's face, and the max operator is globally operated in the entire domain. The $\nabla \alpha / |\nabla \alpha|$ adds the interface unit vector normal to the direction in which $\mathbf{U}_r$ is applied. Since C_α can be any amount ≥ 0, if $C_\alpha \leq 1$, then Eq. (12) becomes (Barbosa et al. 2019):

$$\mathbf{U}_r = C_\alpha |\mathbf{U}| \frac{\nabla \alpha}{|\nabla \alpha|} \tag{13}$$

where C_α in the *multiphaseInterFoam* solver simplifies to a binary coefficient that shifts to 1 for interface sharpening "on" and 0 for "off".

Eulerian model

The most complicated multi-layer model in OpenFOAM is the Eulerian model, where each phase is considered as an interpenetrating layer, and a set of *k* continuity and momentum equations is resolved separately for each phase. The model's computational time is, therefore, much longer than that of VOF, but a specific pressure is allocated by all phases. This model is particularly applicable to flows where fluid boundaries may mix together (interpenetrate) through the process, e.g., multiphase fluids with miscible boundaries. The Eulerian multi-layer method in OpenFOAM enables the modelling of several distinct, yet, interpenetrating layers. The layers may be solids, gases, and liquids in each combination. In this study, such simulations were done using the highly efficient solver *multiphaseEulerFoam*. The multiphase flow equations for k continuous phases solved in the Eulerian model are shown below as a group of continuity and momentum equations (Fluent 2013; Open∇FOAM 2015; Wang et al. 2020b):

$$\frac{\partial \alpha_k \rho_k}{\partial t} + \nabla \cdot (\alpha_k \rho_k \mathbf{U}_k) = 0 \tag{14}$$

$$\frac{\partial \alpha_k \rho_k \mathbf{U}_k}{\partial t} + \nabla \cdot (\alpha_k \rho_k \mathbf{U}_k \mathbf{U}_k) = -\alpha_k \nabla \mathbf{p} + \nabla \cdot \boldsymbol{\tau}_k + \alpha_k \rho_k \mathbf{g}_k + \mathbf{S}_k = 0 \tag{15}$$

where $\mathbf{U}_k$ is the mean velocity field; subscript k refers to the k^{th} continuous phase; $\mathbf{p}$ is the mean pressure; and $\boldsymbol{\tau}_k$ is the k^{th} phase stress tensor, given by (Barbosa et al. 2019):

$$\boldsymbol{\tau}_k = \alpha_k \mu_k [(\nabla \mathbf{U}_k) + (\nabla \mathbf{U}_k)^{\mathrm{T}}] \tag{16}$$

The *multiphaseEulerFoam* solver applies additional limits called "Multidimensional Universal Limiter with Explicit Solution" (MULES) on the result of the phase transport equations to guarantee the phase conservation against the boundedness in the results of hyperbolic problems. (Nilsson 2010). Theoretical details of MULES (Section S2) and comprehensive aspects of the OpenFOAM setup (Section S13) are provided in the Supplementary Materials.

Initial and boundary conditions, and computational domains

Owing to the experimental flume dimensions, the computational area was 6-m long, 0.32-m deep, and 0.3-m wide. Two semi-circular obstacles with 0.045 and 0.075-m radii were specified and positioned 1 m downstream of the dam section. The silted-up flood wave was modelled as a three-phase incompressible system (air-water-sediment layer) using VOF and Eulerian methods, including the influence of kinematic viscosity, density, and surface tension. The simulation input data are given in Table 2. A sloping bed may lead to an increase or decrease in flood wave propagation (Dias and Dutykh 2007), which can be affected by parameters, such as bed roughness (Bocchiola et al. 2006). To keep the numerical models as simple as possible, flume and obstacle sides in connection with the flood wave were assumed to be smooth, and a horizontal bed was used. However, the influence of such factors on silted-up dam-break flood waves require further exploration.

Under the initial conditions, the experimental reservoir (1.52-m long, 0.3-m wide, and 0.3-m deep) was filled to the required level with a saturated sediment deposit. The remainder of the reservoir was filled by sediment-free water, and everything above was deemed air. To define boundary conditions, as there was no lateral inflow, the beginning of the flume, bottom, and side boundaries were chosen as the "*wall functions"*. The static contact angle at the walls was set to 90˚ for all combinations of mixtures in order to avoid the use of the surface tension force between the wall and fluid. The normal vector, $\hat{n}$, to the interface of the wall can be described as (Open∇FOAM 2015):

$$\hat{n} = n_w \cos(\theta_{eq}) - n_t \sin(\theta_{eq}) \tag{17}$$

where n_w is the unit vector pointing towards the wall; θ_{eq} is the static contact angle set to 90˚; and n_t is the unit vector tangential to the wall pointing toward the fluid. The interface of the fluid is then, in fact, normal to the wall. If θ_{eq} is less than 90˚, this would indicate that the fluid wets the wall. The downstream endpoint of the experimental flume was set as a "*pressure outlet"*, and the flume's upper edge was selected as a "*pressure inlet"* considering atmospheric pressure. There was no set contact angle since the fluids should never come in contact with this region. Hence, when the simulation was initiated, the gravitational force led to sudden movement of reservoir's content.

Table 2. The simulation input data

	Units	Name in OpenFOAM	Air	Water	Saturated packed sediment layer
Kinematic viscosity	$\boldsymbol{m^2 s^{-1}}$	nu	$\mathbf{1.48 \times 10^{-5}}$	$\mathbf{1.0 \times 10^{-6}}$	$\mathbf{6.27 \times 10^{-2}}$
Density	$\boldsymbol{kg\, m^{-3}}$	rho	$\mathbf{1.0}$	$\mathbf{1.0 \times 10^{3}}$	$\mathbf{2.08 \times 10^{3}}$

Note: Surface tension or sigma in OpenFOAM was set at $\mathbf{0.07}$ ($\boldsymbol{N\, m^{-1}}$).

Computational meshes and time steps

In this study, 8 mesh sizes (30, 25, 20, 15, 10, 5, 3.3, and 2.5 mm) were adopted to analyse the results. Considering the error values and runtimes, rectangular cube cells with a length, width, and depth of 0.005 m were designated. Hence, the resulting 3D solution domain was discretized into a total of 4.6 million cube cells. A finer variable mesh size (up to 2 mm) was applied as it approached the obstacle's crest at an interval of 0.1 m before and after the obstacle to better simulate that region. After rigorously analysing several distinct time steps (0.01, 0.005, 0.001, and 0.0005 s), a constant time step of 0.001 s was adopted due to the error values, runtime, and the courant number. Comprehensive details of time step and mesh size analyses are provided in the Supplementary Materials (Section S14).

In order to validate the experimental records and OpenFOAM predictions, a specific dam-break scenario was modelled both numerically and experimentally with various downstream hydraulic conditions: initially dry or wet downstream (Vosoughi 2018). Results were evaluated through comparison with an experimental study (Ozmen-Cagatay and Kocaman 2010). Accordingly, Fig. 4, depicts a group of photograph-based comparisons at several snap-times following the failure of the dam, to visually assess the outcomes of the current research compared to other research results. Figs. S3 and S4 (see Supplementary Materials) compare the numerical predictions of OpenFOAM both visually and quantitatively with available experimental measurements (LaRocque et al. 2013). A group of VOF replication results at a reservoir initial sediment height of 0.015 m and with an obstacle radius of 0.045 m located downstream is described in the Supplementary Materials (Fig. S7).

RESULTS

Experimental results

Fig. 5 displays a set of experimental images that can serve as a visual comparison of sediment depth and free surface water level profiles for different initial reservoir sediment depths. All images were extracted from two specific time snaps, 0.5 and 0.8 s after dam failure, in the presence of a downstream semi-circular obstacle with a radius of 0.045 m. As the reservoir sediment layer height increased, the flood wave propagated more slowly. For instance, for the water-filled reservoir (sediment-free) at 0.5 s after the dam-break, the flood wave had already hit and passed over the obstacle by about 0.8 m; however, with initial reservoir sediment layer heights of 0.22 and 0.24 m, the wave had not even reached the obstacle. The wave’s tip was thrown up and forward after it hit the obstacle, and the sediment layer stretched and dampened as it advanced downstream. A further set of experimental video images was classified for all different upstream sediment depths and a semi-circular obstacle of radius 0.075 m, which is presented in the Supplementary Materials (Fig. S6).

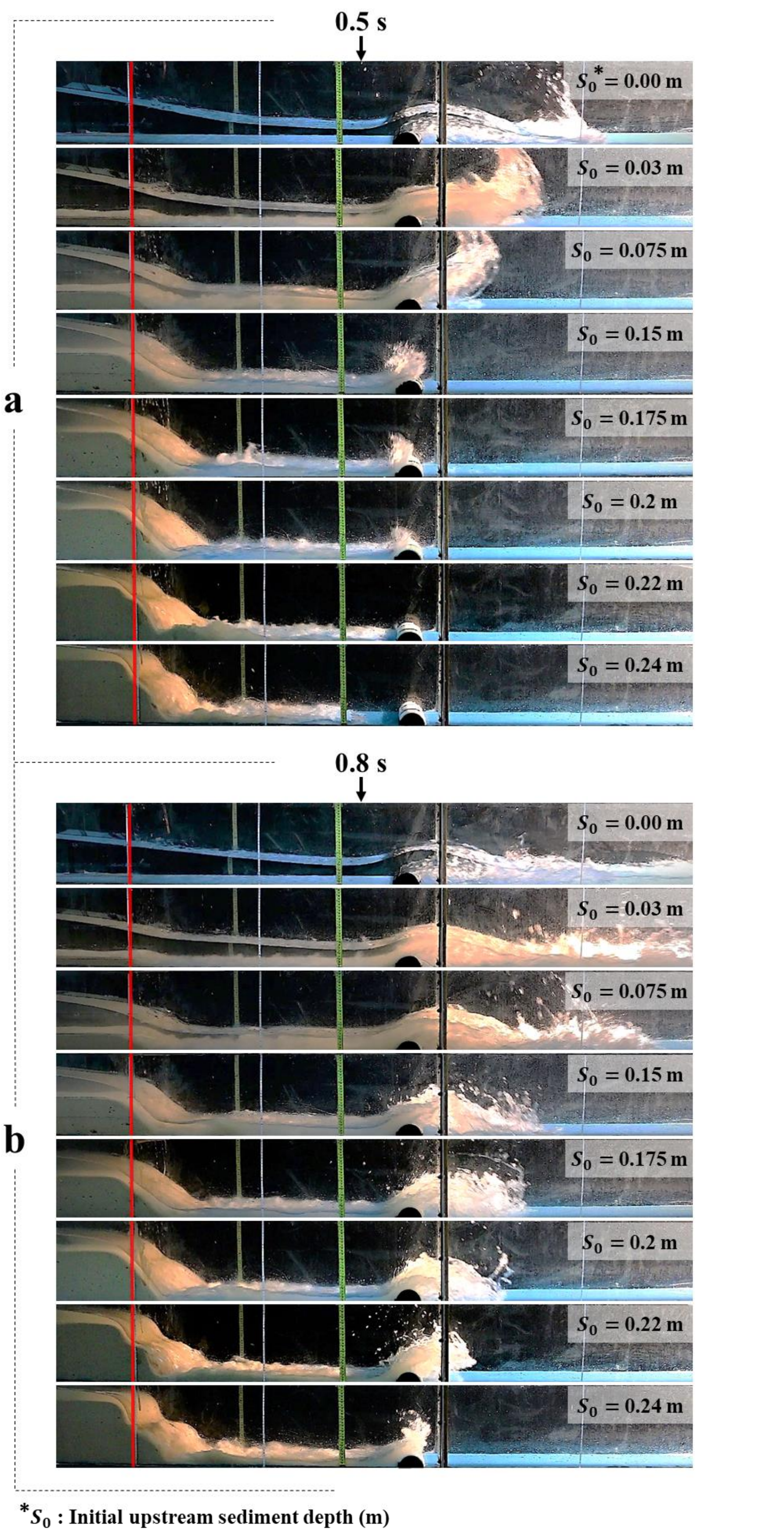

Fig. 5. A visual comparison of experimental images at 0.5 s (a) and 0.8 s (b) after dam break, for 8 different initial upstream sediment depths ($\boldsymbol{S_0}$); 0, 0.03, 0.075, 0.15, 0.175, 0.2, 0.22 and 0.24 m, when a semi-circular obstacle with radius 0.045 m is located downstream. A vertical line represents the gate section

369 Figures 6a-f present six sets of ternary images taken 6, 5, 4, 3, 2, and 1 s after the dam-break at six

distinct upstream sediment depths (0, 0.03, 0.075, 0.15, 0.2 and 0.24 m). Three different downstream conditions were evaluated: no obstacle (top image), obstacle with a radius of 0.045 m (middle image) and obstacle with a radius 0.075 m (bottom image). Figs. 6a-c show that the water level dropped significantly after passing the obstacle, compared to the water level in the absence of an obstacle. Although the larger obstacle led to a shallower flood downstream, the flood wave before the obstacle was proportionately deeper (Figs. 6a-d). As the downstream obstacle increased in height, the dam-break wave propagated more slowly, and the front wave celerity subsequently decreased (Fig. 6f).

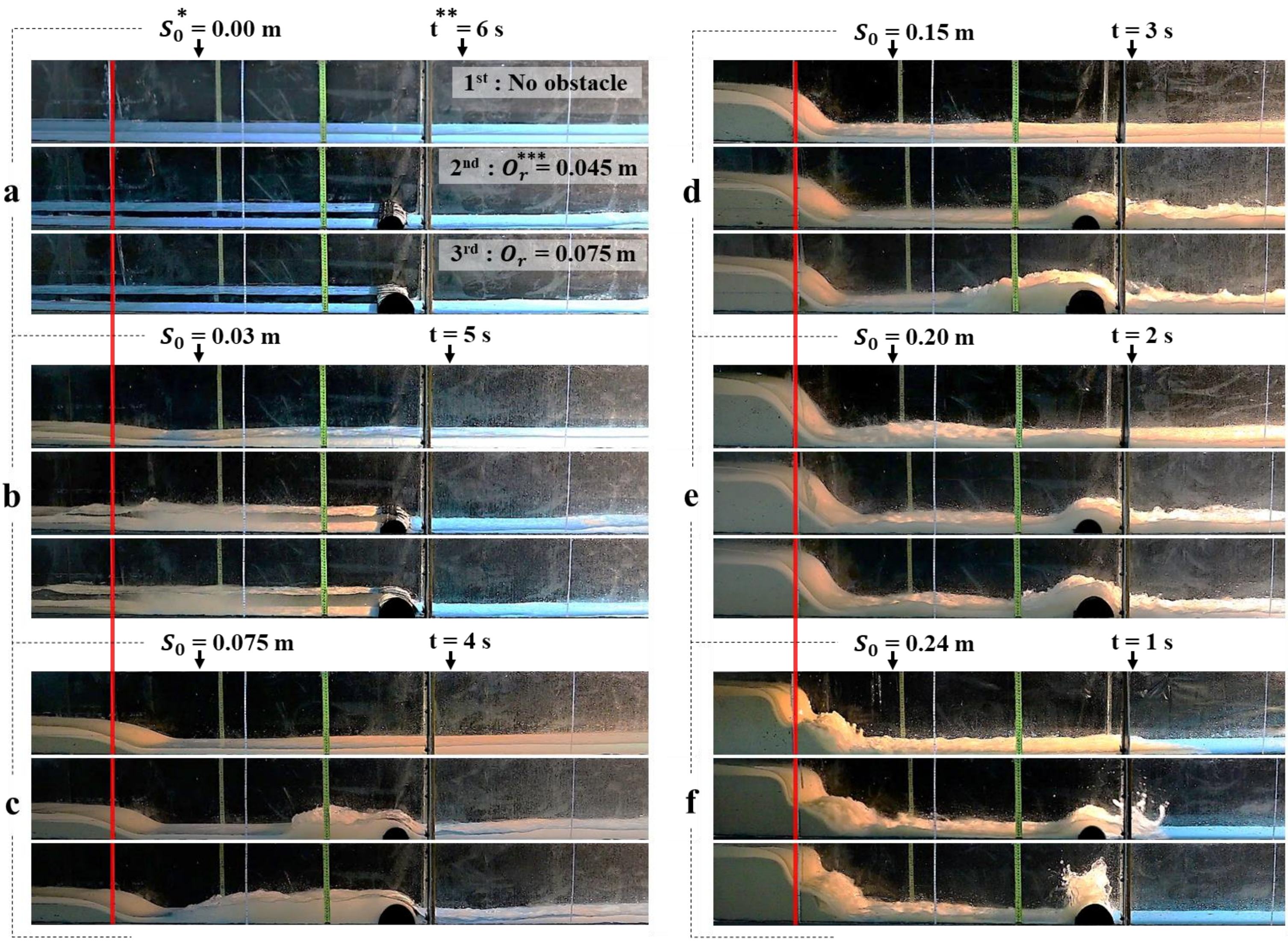

$^*S_0$: Initial upstream sediment depth (m); **t : The time after dam break (s); $^{***}O_r$: The obstacle's radius (m)

Fig. 6. Six sets of ternary images, each showing 3 different downstream conditions; absence of obstacle, presence of semi-circular obstacle with radius of 0.045 and 0.075 m. For different times of 6, 5, 4, 3, 2, and 1 s after dam-break and upstream sediment depths of 0, 0.03, 0.075, 0.15, 0.2 and 0.24 m respectively (a-f). A vertical line represents dam section

Using video images, front wave celerity values were carefully measured at four intervals, each 1 m in length, along the flume portion downstream from the dam. The first downstream interval ranged 1.52-2.52 m from the beginning point of the reservoir, and the other intervals were 2.52-3.52, 3.52-4.52, and 4.52-5.52 m. The values of front wave celerity in the mentioned intervals are classified in Tables S2-S4, one for each of downstream condition, in Section S7 of the Supplementary Materials, with additional technical details. The average computed dam-break front wave celerity along the downstream channel for the 24 different scenarios are presented in Table 3.

Table 3. Average computed front wave celerity through the channel (m/s)

Average front wave celerity (m/s)			
Initial depth of sediment in the reservoir (m)	Downstream initial condition		
	No obstacle	Obstacle with 0.045 m radius	Obstacle with 0.075 m radius
0	2.32	2.13	2.10
VAR	0.01	0.01	0.02
0.03	2.26	2.08	2.01
VAR	0.01	0.02	0.03
0.075	2.17	1.94	1.90
VAR	0.01	0.02	0.04
0.15	2.04	1.70	1.65
VAR	0.01	0.06	0.08
0.175	1.92	1.60	1.53
VAR	0.01	0.08	0.10
0.20	1.75	1.52	1.42
VAR	0.03	0.08	0.11
0.22	1.65	1.42	1.35
VAR	0.02	0.06	0.09
0.24	1.28	1.20	1.03
VAR	0.04	0.06	0.10

Note: VAR = Variance value (m^2/s^2).

Based on Table 3, the initial depth of reservoir sediment strongly influenced wave celerity: the greater the initial reservoir sediment depth, the slower the shock wave progression. Lower water depths on top of the sediment coat led to a decrease in celerity of the front wave. The presence of a downstream obstacle also led to a reduction in multiphase wave celerity once the shock wave hit the obstacle, where the taller obstacle reduced the front wave celerity more than the shorter obstacle. In all scenarios, the mean front wave celerity values caused by the dam-break along the flume varied from 1 to 2.3 m/s, depending on the upstream and downstream initial hydraulic conditions. The variances of all average celerity values are presented in Table 3 (VAR line). The computed variances were minor and fluctuated between 0.01 and 0.1 m^2/s^2. The maximum variance occurred in the scenarios where the flood depth suddenly dropped due to the presence of a downstream obstacle, resulting in a noticeable decrease in wave celerity.

Comparison of experimental measurements and numerical results

As described in the Experimental Modelling section, a total of 20 positions along the channel and 15 time-snaps following dam-break were selected to obtain the required data. A short distance between two adjacent locations along the dam was set to capture the sudden depth changes and high turbulence in that region. Once the dam-break occurred, the intervals between time snaps were brief and then increased with time.

Flow pattern comparison

Image comparisons provided in this section and the Supplementary Materials (Section S8) visually illustrate the experimental and numerical conditions. The images were depicted below each other for 8 different times (0, 0.1, 0.2, 0.3, 0.4, 0.6, 0.8, and 1 s) after the dam-break. A channel section about 2.2 m in length was covered by the images (1.32 to 3.52 m from the beginning point of the reservoir). Fig. 7 depicts an image comparison when the reservoir initial sediment height was 0.075 m and a semi-circular obstacle with a radius of 0.075 m was mounted downstream. Experimental images and VOF and Eulerian predictions are depicted below each other at the appropriate and comparable positions.

As can be seen from Figs. 7g-i, at 0.2 s, the flood wave reached 0.5 m downstream from the dam and the water level dropped about 7 cm at the dam section. At 0.8 and 1 s, the sediment coat had progressed about 13 cm downstream, and the sediment depth at the dam section decreased about 3 cm (Figs. 7s and v). For the VOF vs Eulerian predictions at 0.8 and 1 s, it is evident that the amount of sediment movement downstream and its depth at the dam section were similar. Although experimental records and both numerical results were in good agreement, the Eulerian method seemed to be more accurate in simulating this situation. Fig. S10 compares a set of experimental images to VOF results for a case with a water-filled reservoir (sediment-free) and a semi-circular obstacle of radius 0.045 m located downstream from the dam. Fig. S11 shows a similar comparison when the reservoir initial sediment height was 0.03 m.

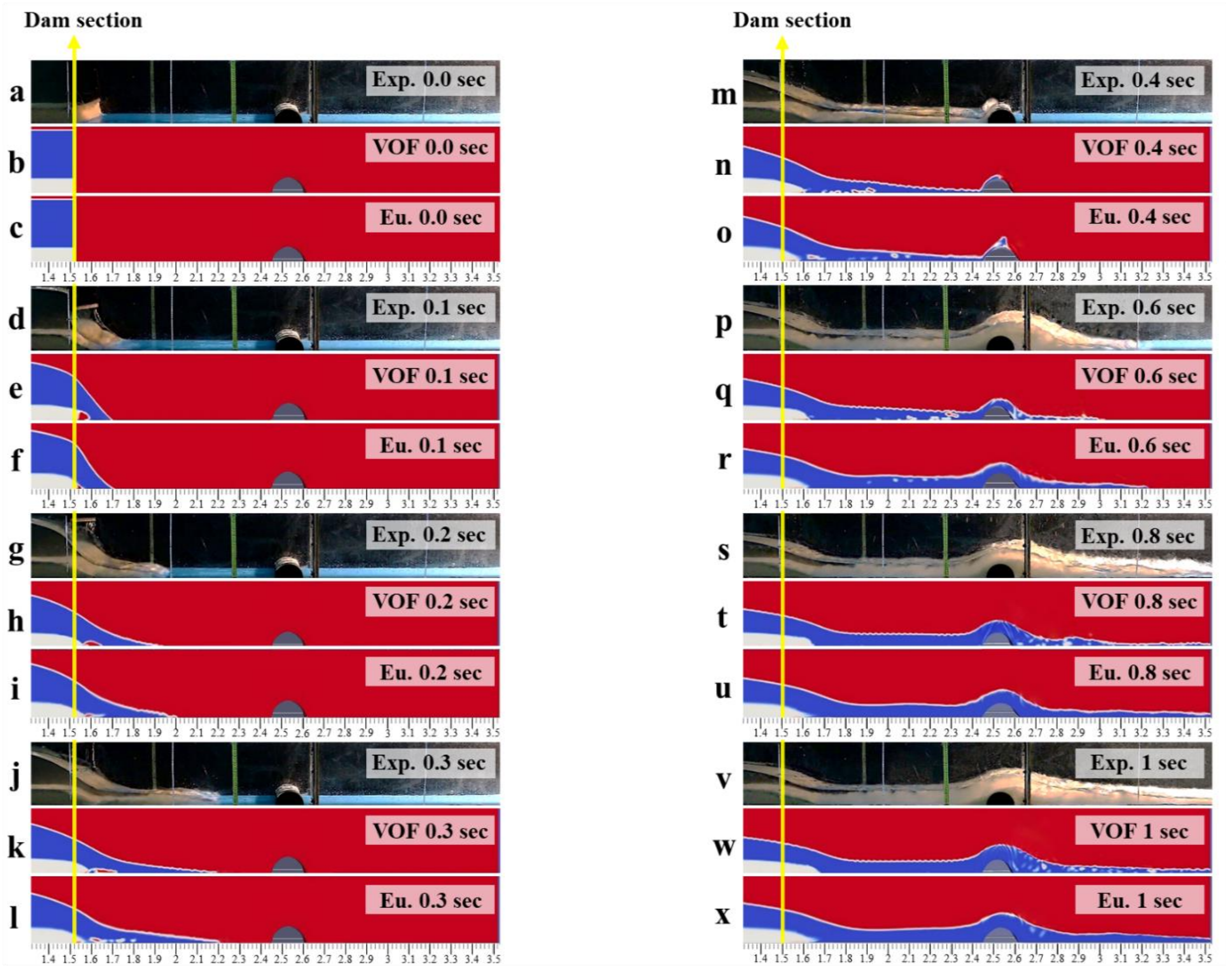

Fig. 7. Image-based comparison of experimental records (a, d, g, j, m, p, s & v) versus VOF (b, e, h, k, n, q, t & w) and Eulerian results (c, f, i, l, o, r, u & x) indicating sediment depth and water level profiles, at various time snaps: 0 (a, b & c), 0.1 (d, e & f), 0.2 (g, h & i), 0.3 (j, k & l), 0.4 (m, n & o), 0.6 (p, q & r), 0.8 (s, t & u) and 1 (v, w & x) seconds. The reservoir initial sediment depth was 0.075 m and a semi-circular obstacle with radius of 0.075 m is mounted downstream from the dam. The vertical line represents the dam section

Sediment depth and free surface water level profiles

A selection from the large number of sediment depth and water level profiles based on data extracted from video images is presented in this section to evaluate the influence of downstream semi-circular obstacles on the multiphase flood wave propagation. All graphs represent both measured data (points) and numerical predictions (lines). The $h_t/h_0(-)$ ratio represents the nondimensional water level, where h_t is the height of the water at a particular time along the channel and h_0 is the initial reservoir water height (0.3 m in all cases). The ratio $S_t/S_0(-)$ is the nondimensional sediment depth, where S_t is the sediment depth at a particular time along the flume and S_0 is the initial upstream sediment depth.

Fig. 8 depicts the experimental vs VOF results in estimating the free surface water profile along the channel when the reservoir was filled with sediment-free water. Six distinct times after the dam-break are illustrated in Fig. 8: early times (0.04 and 0.2 s) and later times (0.4, 1, 2 and 6 s). Two different semi-circular obstacles with a radius of 0.045 m (a and c) or 0.075 m (b and d) were located 1 m downstream from the dam. The wave generated by the dam-break created a huge bulge after hitting the obstacle and passing over it. The taller the obstacle, the larger the bulge created in the flood wave and, consequently, the shallower the flood after the obstacle (Figs. 8c and d). Moreover, it seems that smaller changes occurred immediately after the dam-break (Figs. 8a and b). Considering the lack of significant statistical error values, there was a strong concurrence between the experimental and VOF results. The highest Mean Absolute Error (MAE) and Root Mean Square Error (RMSE) values were 0.009 and 0.012 m, respectively, which were negligible relative to $h_0 = 0.3$ m.

Figures 9 shows the VOF (a and c) and Eulerian (b and d) predictions vs experimental measurements at three time-snaps following the dam-break: 0.4, 2 and 6 s. Figure 9 also compares VOF (a) and Eulerian (b) results in determining the free surface water level profile when the initial sediment height in the reservoir was 0.15 m and a semi-circular obstacle with a radius of 0.045 m was mounted downstream. Both numerical methods and measured data were in agreement. The highest MAE and RMSE occurred for VOF results with values of 0.0174 and 0.026 m, respectively, and were very low compared to $h_0 = 0.3$ m. Considering the values of statistical error indices, the Eulerian showed better concurrence with measured data than the VOF method. As can be seen, at 2 s, the water level increased sharply at the downstream obstacle location, then suddenly dropped after it, which was predicted well by both VOF and Eulerian methods.

An evaluation of the numerical outcomes in matching the measured sediment depth profile (Figs. 9c and d) for a reservoir initial sediment depth of 0.2 m and a semi-circular obstacle with radius 0.075 m mounted downstream showed the Eulerian method (max. RMSE = 0.0307 m and max. MAE = 0.0179 m) outperformed VOF (max. RMSE = 0.0366 m and max. MAE = 0.0228 m). Assuming the reservoir sediment coat to be a viscid fluid in numerical modelling, the outcomes were plausible. VOF predictions indicated that, 6 s after the dam failure, the sediment layer had reached the obstacle and accumulated behind it (Fig. 9c). In comparison, the Eulerian predictions suggested that the sediment layer had reached a position just slightly before the obstacle (Fig. 9d.)

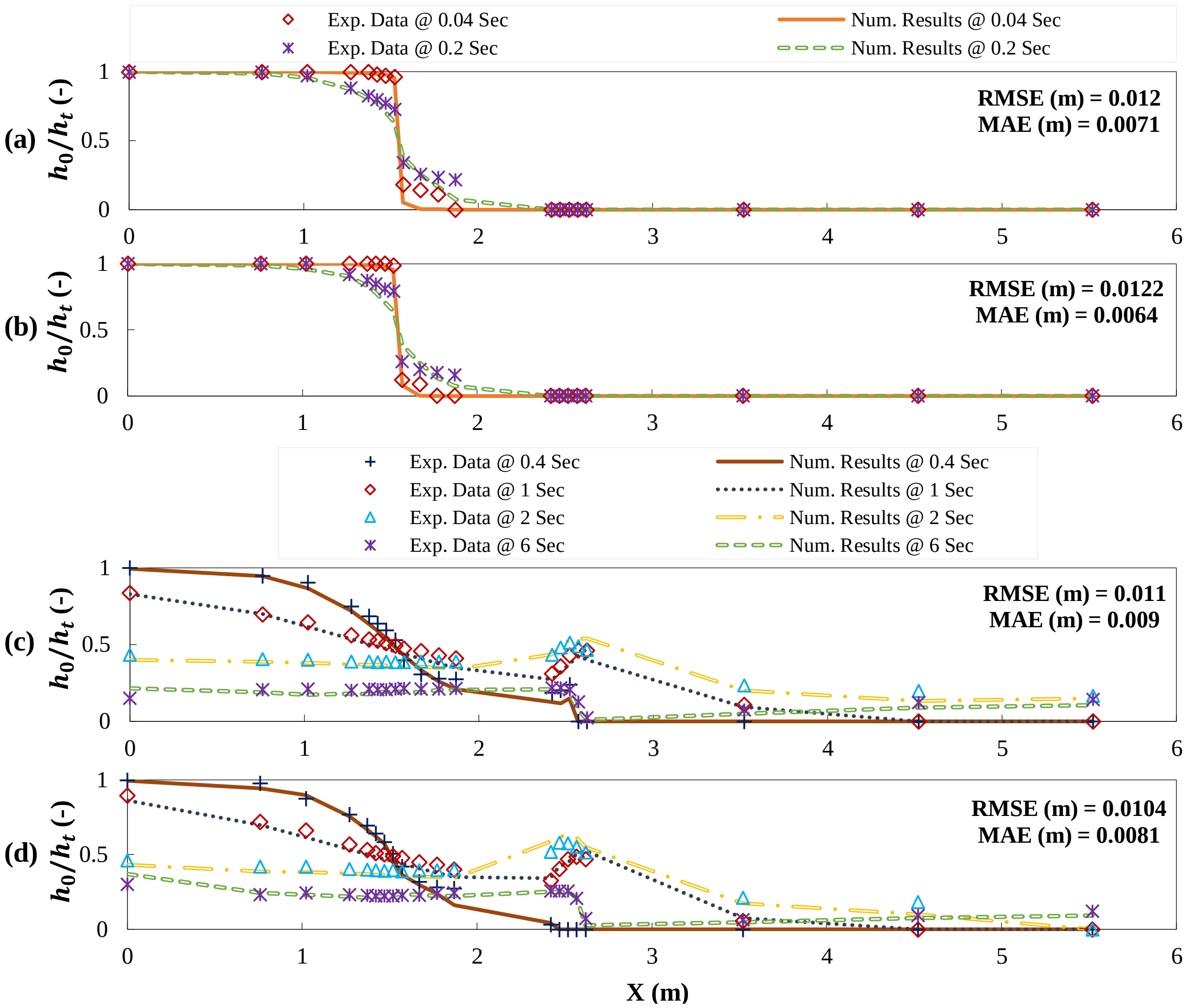

Fig. 8. Laboratory records vs VOF estimations in determining the water level profiles at distinct times; (a & b) 0.04 and 0.2 s, (c & d) 0.4, 1, 2 and 6 s. The reservoir was filled by sediment-free water and a semi-circular obstacle with a radius of 0.045 m (a & c) or 0.075 m (b & d) was mounted downstream from the dam. Dashed lines represent dam and downstream obstacle sections, respectively. $h_t/h_0(-)$ is nondimensional water level along the flume, where $h_0 = 0.3\ m$

In general, comparisons with measured data demonstrate better Eulerian performances than VOF, particularly in simulating a silted-up dam-break wave for a highly-silted reservoir and in modelling multiphase flood wave propagation over a bumpy bed. Despite its better prediction accuracy, the

Eulerian approach suffers from longer computational times and more complex simulation conditions, as shown in Table S6 (run times) in the Supplementary Materials (Section S11).

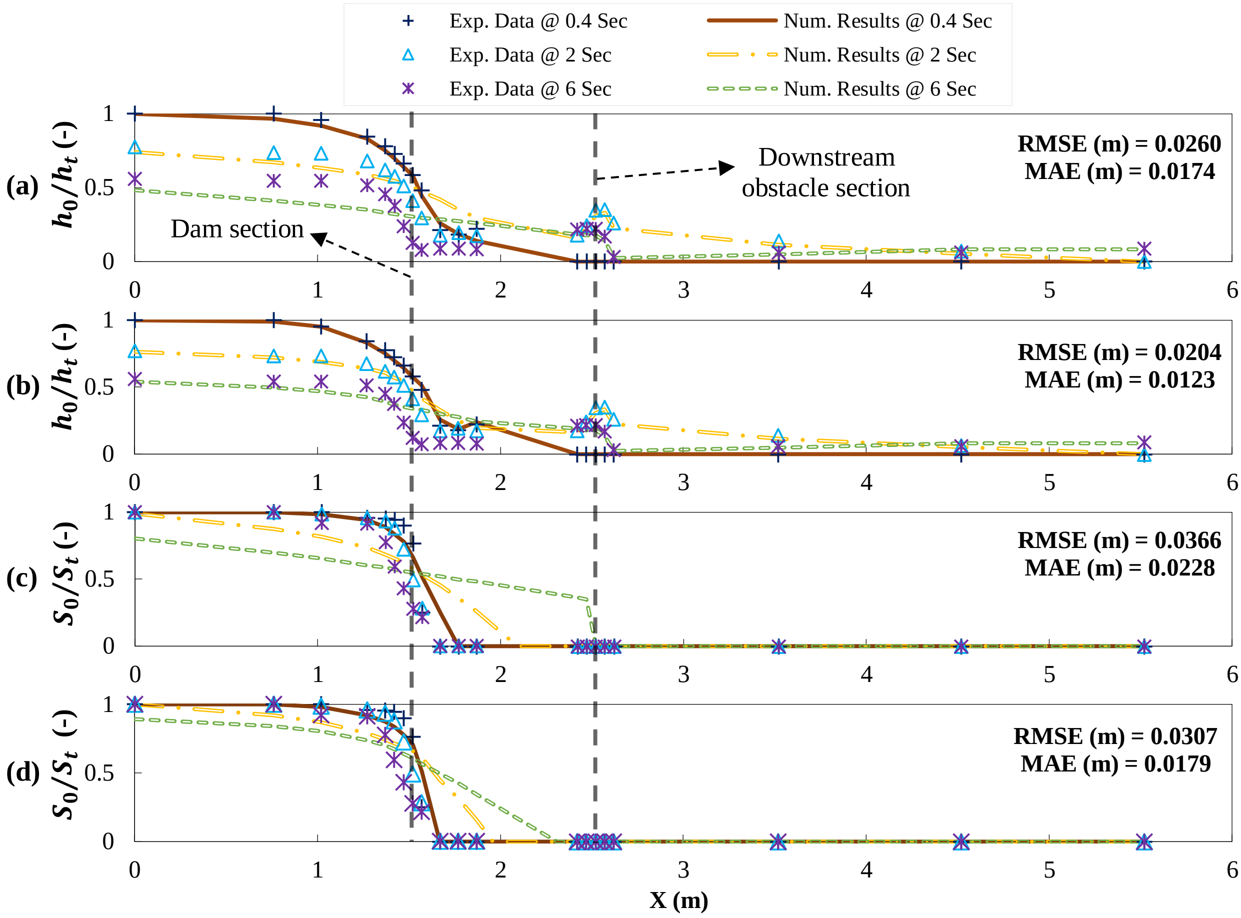

Fig. 9. Experimental measurements *vs*. both VOF (a & c) and Eulerian predictions (b & d) in determining profiles of water level (a & b) and sediment depth (c & d) at various time snaps of 0.4, 2 and 6 s. Reservoir initial sediment depth is 0.15 m (a & b) or 0.2 m (c & d). A semi-circular obstacle with radius of 0.045 m (a & b) or 0.075 m (c & d) is mounted downstream from the dam. Dashed lines represent dam and downstream obstacle sections, respectively. $h_t/h_0(-)$ and $S_t/S_0(-)$ are nondimensional water level and sediment depth along the flume and $h_0 = 0.3\ m$

Table 4 compares the RMSE and MAE values of the prediction of free surface water level profiles under all various initial upstream and downstream conditions and at four time-snaps after the dam-break (0.4, 1, 2, and 6 s). The highest RMSE and MAE were found using the VOF method when the reservoir initial sediment depth was 0.22 m. The table illustrates that the greater the reservoir initial sediment height, the higher the reported error values. Assuming the sediment layer to be a viscous fluid played a major role in increasing the error values due to an increase in the upstream sediment depth. However, both numerical methods had good performances in predicting more complicated downstream-bed hydraulic conditions. According to Table 4, the reported error values of the Eulerian method were smaller in most scenarios, and there was a higher visual concurrence between the experimental measurements and Eulerian results than those of VOF. Additional error values of VOF and Eulerian outcomes in estimating sediment depths are shown in Table S5 in the Supplementary Materials. Based on Tables 4 and S5, it can be concluded that the Eulerian results were more accurate and better matched the recorded data than VOF in estimating sediment depth and water level profiles, especially when more than half of the reservoir depth was initially filled by sediment (≥ 0.15 m).

Table 4. The statistical error values in estimating free surface water level profiles via VOF and Eulerian numerical methods computed using four different times after the dam break; 0.4, 1, 2 and 6 s

Downstream hydraulic conditions	Numerical methods	Statistical error indices	Upstream sediment depth (m)							
			0.00	**0.03**	**0.075**	**0.15**	**0.175**	**0.2**	**0.22**	**0.24**
No obstacle	VOF	RMSE (m)	0.0035	0.0131	0.0094	0.0315	0.0320	0.0381	**0.0411**	0.0403
		MAE (m)	0.0028	0.0099	0.0069	0.0228	0.0231	0.0276	**0.0305**	0.0293
	Eulerian	RMSE (m)	−	0.0085	0.0087	0.0234	0.0284	0.0357	0.0345	0.0387
		MAE (m)	−	0.0073	0.0064	0.0166	0.0195	0.0234	0.0239	0.0282
Obstacle with radius of 0.045 m	VOF	RMSE (m)	0.011	0.0099	0.0108	0.0260	0.0291	0.0339	0.0373	0.0372
		MAE (m)	0.009	0.0073	0.0078	0.0174	0.0200	0.0223	0.0261	0.0271
	Eulerian	RMSE (m)	−	0.0084	0.0098	0.0204	0.0279	0.0295	0.0346	0.0360
		MAE (m)	−	0.0063	0.0068	0.0123	0.0164	0.0179	0.0216	0.0247
Obstacle with radius of 0.075 m	VOF	RMSE (m)	0.0104	0.0076	0.0111	0.0228	0.0253	0.0287	0.0360	0.0387
		MAE (m)	0.0081	0.0060	0.0081	0.0149	0.0168	0.0193	0.0253	0.0279
	Eulerian	RMSE (m)	−	0.0073	0.0099	0.0183	0.0244	0.0251	0.0345	0.0360
		MAE (m)	−	0.0051	0.0067	0.0122	0.0164	0.0170	0.0211	0.0244

Note: RMSE = Root Mean Square Error; MAE = Mean Absolute Error.

Sediment depth and water level variations over time

Sediment depth and water level variations after a dam-break event were investigated at three control points along the flume (0.76, 1.52 and 2.52 m from the reservoir's beginning point). A schematic 3D view of the flume with these control points is depicted in the Supplementary Materials (Fig. S12). Figures 10a and b present the comparisons of measured data and VOF results in estimating water surface changes by elapsing time after a dam-break event when a semi-circular obstacle with a radius of 0.045 m (a) or 0.075 m (b) was positioned downstream of the dam.

The VOF predictions and measured data fit well, and the highest MAE and RMSE values were 0.007 and 0.0109 m, respectively. The values varied from 2.2% to 3.6% for $h_0 = 0.3$ m. As shown in Fig. 10a and b, the error indices increased as the downstream semi-circular obstacle became taller. At the first control point in the middle of the reservoir (0.76 m), the water level dropped slowly until 4 s and then increased due to a negative wave generated by the downstream obstacle. The water surface at the second control point (dam location) dropped rapidly once the dam-break occurred then decreased slowly until the negative wave developed. Fig. 10a and b show that the higher the obstacle, the deeper and faster the negative wave was generated. At the third control point (obstacle section), the water level increased until 2 s and then decreased slowly and steadily. The maximum water level at the third control point was 0.15 m when a 0.045-m tall obstacle was mounted in the downstream bed and was 0.175 m for a 0.075-m tall obstacle.

Figures 10c-f depict the sediment depth and water level variations over elapsed time after dam failure at the three control points along the flume using measured VOF (c and e) and Eulerian estimation (d and f) data. As illustrated in Figures 10c and d, the initial height of the sediment layer in the upstream reservoir was 0.175 m, and a downstream obstacle had a radius of 0.045 m. Reservoir sediment with an initial height of 0.24 m and obstacle with a radius of 0.075 m are presented in Figs. 10e and f, respectively. According to Figures 10c-f, VOF and Eulerian estimates were in adequate agreement with recorded data. The highest MAE and RMSE were 0.0246 and 0.0351 m, respectively, for the VOF and were improved upon under the Eulerian approach (0.0304 and 0.0208 m). As the initial upstream sediment became deeper, the statistical error indices increased. The nondimensional parameter of $\frac{y_t}{y_0}\,(-)$, which is presented on the vertical axes in Figs. 10c-f, represents both $h_t/h_0\ (-)$ and $S_t/S_0\ (-)$.

At the first control point (0.76 m) in Figs. 10c and d, the water level decreased slowly after the dam-break, and the sediment coat transformed insignificantly. However, at the dam section (second control point), the sediment depth and water level changed rapidly immediately after the failure of the dam and then decreased slowly. The water level at the third control point (downstream) increased until 2 s then decreased slowly. For the 80% silted-up reservoir (Figs. 10e and f), all analyses were similar to those in Figures 10c and d. However, at 3 s, the water level increased then decreased again under the influence of the negative wave due to the downstream obstacle.

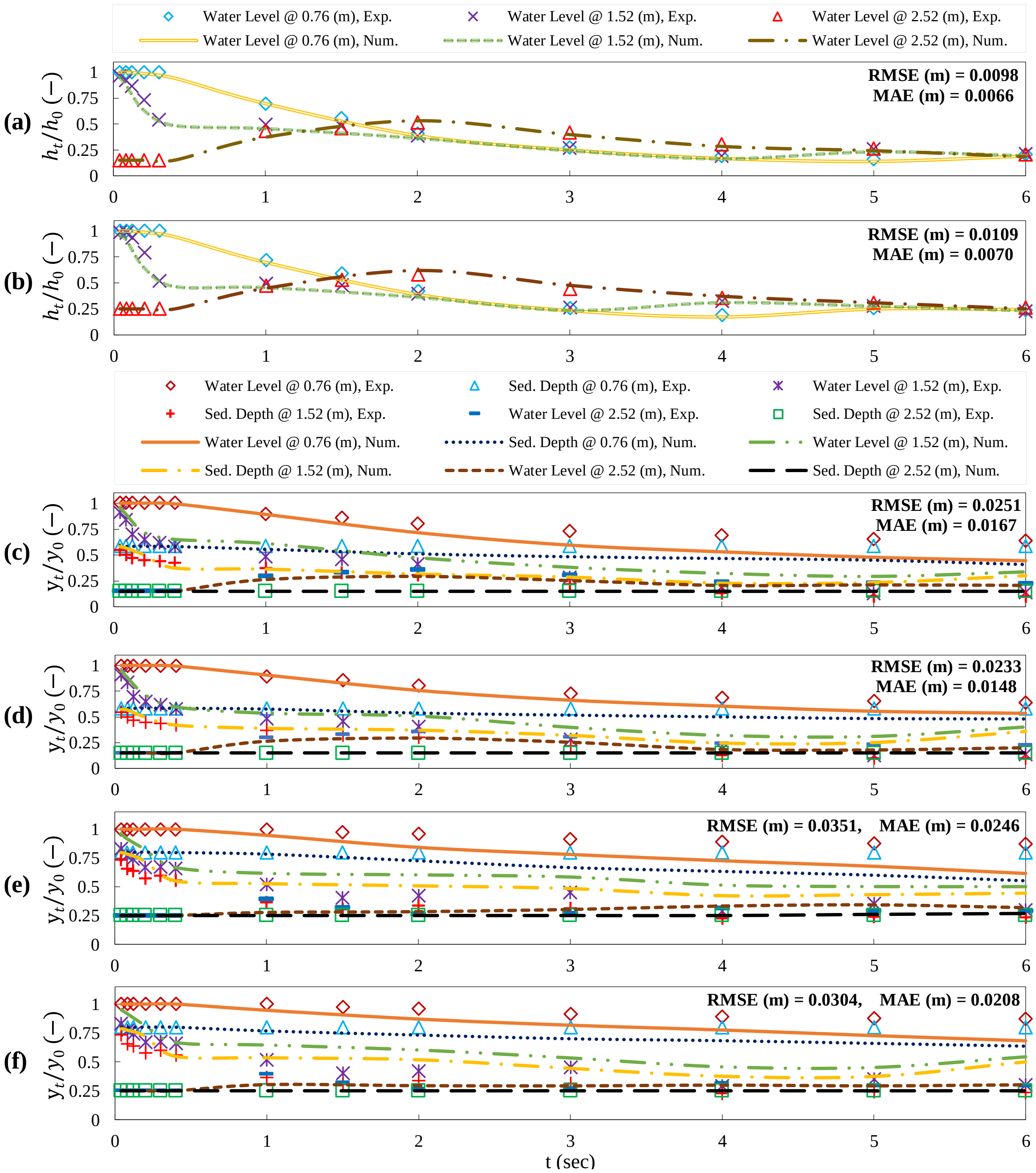

Fig. 10. A comparison of experimental measurements with VOF (a, b, c & e) and Eulerian results (d & f) in estimating sediment depth and water level variations over elapsed time at 3 control points along the flume; 0.76 m (the reservoir mid-point), 1.52 m (gate section) and 2.52 m (obstacle section). Initial height of sediment in reservoir is 0.00 m (a & b), 0.175 m (c & d) or 0.24 m (e & f), and a semi-circular obstacle with radius of 0.045 m (a, c & d) or 0.075 m (b, e & f) is mounted downstream from the dam. The nondimensional parameter of y_t/y_0 $(-)$ at the vertical axes of figures c, d, e and f, represents both h_t/h_0 $(-)$ and S_t/S_0 $(-)$. $h_0 = 0.3\ m$

Correlation analysis of measured data and numerical predictions

Figure 11 depicts the correlation between laboratory data and numerical outcomes by VOF (a and b) and Eulerian methods (c) using the Coefficient of Determination (R^2) as a correlation index. The horizontal axes represent experimental data, while the vertical axes depict numerical results in determining water level values at 20 positions in the flume at 7 time-snaps. Fig. 11a presents the case where the reservoir was filled by sediment-free water, and a 0.075 m radius obstacle was mounted dowstream from the dam. Here, the VOF results were highly correlated with measured data (R^2 = 0.9851). The correlation between laboratory records with VOF (Fig. 11b) and Eulerian (Fig. 11c) results, when the initial height of reservoir sediment was 0.15 m and the obstacle had a radius of 0.045 m, indicated that both VOF and Eulerian predictions were highly correlated with measured data. R^2 values were 0.9402 and 0.9631, respectively, indicating that the Eulerian approach provided a closer match than the VOF method. The opportunity of mixing the boundaries between layers in the Eulerian method might have explained its better outcome.

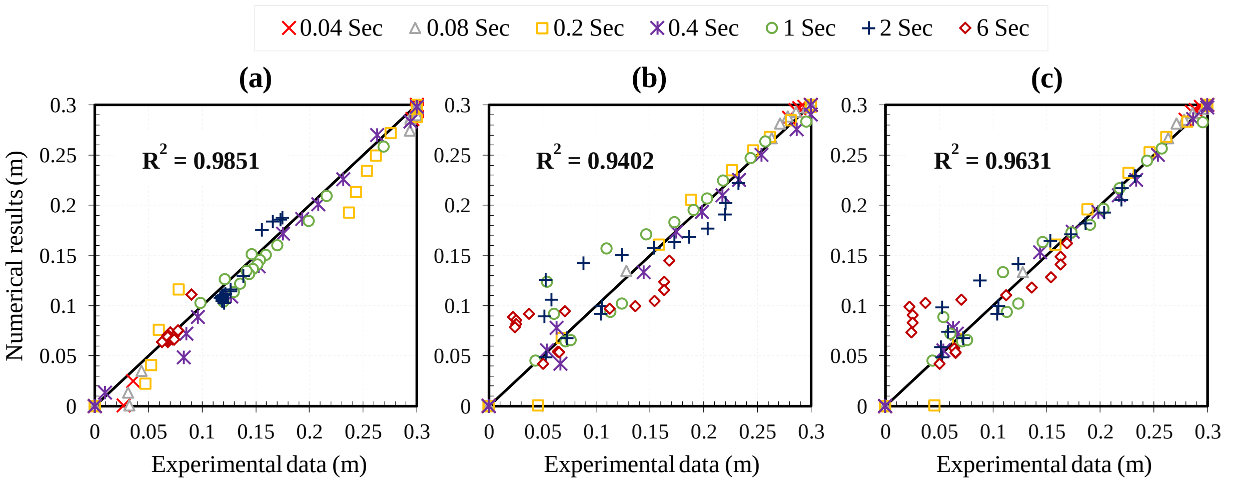

Fig. 11. Correlation analyses of experimental measurements and VOF (a & b) or Eulerian results (c) for different upstream and downstream conditions; (a) the upstream channel is filled up by sediment-free water with a 0.045-m-high downstream obstacle, (b & c) the upstream initial sediment height is 0.15 m with a 0.075-m-high downstream

Run time analysis

A comparison of the required run times between the VOF and Eulerian approaches for all 24 scenarios are shown in Table S6 in the Supplementary Materials (Section S11). For VOF simulations, run times ranged from 5.96 to 31.42 h using a PC notebook with an Intel Core i5-4200U 2.3 GHz, 6 GB RAM, 64-bit processing system for a modelling duration of 10 s. For Eulerian simulations, run times ranged from 13.02 to 52.02 h, which are far longer than those of VOF (Table S6). Hence, the VOF method may be more attractive for wide-scale computational domains considering its simulation simplicity and less computational effort or time compared to the Eulerian approach.

CONCLUSIONS

Upon a dam's failure, the influence of the massive movement of sediment deposited behind the dam caused by a sudden dam-break flood wave is of great importance. Evaluating the effect of a downstream semi-circular obstacle on such a complex phenomenon is vital as it leads to a better technical and practical understanding of the effect of sudden variations in topography in flood-prone areas. As far as we are aware, this topic has never been examined, either experimentally or numerically, in prior research. In this study, the influences of the presence or absence of downstream humps (semi-circular obstacles) on multiphase shock flood waves, caused by the failure of dams with different levels of reservoir silting, were investigated experimentally and verified numerically for a total of 24 dam-break scenarios. The multiphase flood shock wave was recorded by high-speed digital cameras positioned alongside the flume. Sediment layer depths, free surface water levels, and front wave celerity values at various locations and times were extracted by means of image processing. For this purpose, 20 distinct positions along the channel and 15 time-snaps following the dam-break were examined. This multiphase complex flood wave over a downstream obstacle was simulated by OpenFOAM using two numerical methods: VOF and Eulerian. Numerical results were rigorously compared with measured data.

Numerical predictions were in close agreement with measured data, with statistical error indices varying between 0.003 and 0.041 m. The lack of leakage from the edges of the gate, its rapid time of release (0.08-0.16 s), and good-quality recording may contribute to this agreement. The Eulerian approach offered better (3% to 25%) performances than the VOF, particularly for scenarios with deep initial sediment coats ($S_d \geq 0.15$ m). The possibility of simulating the mixing of boundaries between phases under the Eulerian approach may explain its better results. However, the Eulerian method required computational times that were 2-fold greater than the VOF method (Table S6).

Upstream sediment depth was a highly influential factor with respect to celerity of the flood wave. The deeper the initial sediment coat, the more gently the shock wave progressed, most likely because of the difference between the faster water velocity and slower sediment layer propagation velocity. However, as the initial sediment coat became deeper, the sediment coat moved forward more rapidly after the dam-break, and its depth increased proportionally in the downstream area. This may intensify the burial risk of infrastructure located downstream of the dam.

Bumpy downstream reaches in a natural terrain or the artificial creation of such conditions at a specified distance in the downstream bed may extensively affect the physical characteristics of the dam-break flood wave. Such conditions can lead to a significant reduction in shock wave celerity, sediment layer propagation and flood depth downstream of the obstacle. Considering all scenarios, the mean front wave celerity varied between 1.0 and 2.3 m/s (Table 3). As the front wave celerity decreased, the destructive power of the flood decreased accordingly. The presence of a downstream obstacle led to reductions in front wave celerity, and taller downstream obstacles reduced celerity to a greater extent than shorter obstacles. Thus, different upstream and downstream conditions can change the front wave celerity by up to 230%. However, the area between the dam and obstacle location may be the most hazardous and insecure zone after the dam-break, as this is where the deepest sediment layer as well as the highest water level are located. Therefore, it is highly inappropriate to position and maintain any expensive equipment or infrastructure or to construct any office or residential buildings in this area.

In conclusion, the Eulerian method, despite its more accurate predictions, has drawbacks, such as longer computation time and more complicated modelling conditions. Accordingly, the VOF method, given its comparative simulation simplicity and lesser computational needs and time, may be more attractive for wide-scale computational domains. It is noteworthy that collections of original data are accessible online in the public repository accompanying this article (Vosoughi et al. 2021a; b; c).

A key component in upcoming research to explore the effects of upstream sediment on flood propagation would be to include distinct kinds of sediments using different grain sizes or consider suspended and bed load in a saturated sediment layer. It is suggested that future research assess the application of expert systems on estimating such phenomena. Comparing the potential effects of different obstacle shapes on multi-layer shock flood wave propagation would also be a valuable part of future studies. Moreover, simulating the upstream sediment coat as mixtures of particles and water could prove to be important.

SUPPLEMENTARY MATERIAL

See Supplementary Material for the complete details of the study.

DECLARATION OF INTERESTS

The authors declare that they have no known competing financial interests or personal relationships that could have appeared to influence the work reported in this paper.

DATA AVAILABILITY STATEMENT

All data, models, and codes generated or used during the study are available online in a public repository or appear in the submitted article (Vosoughi et al. 2021a; b; c). DOIs:

1- https://doi.org/10.6084/m9.figshare.13686142
2- https://doi.org/10.6084/m9.figshare.13686205
3- https://doi.org/10.6084/m9.figshare.13677454

AUTHORS' CONTRIBUTIONS

Authors	Contribution
Foad Vosoughi	Conceptualization, Software, Validation, Investigation, Resources, Data Curation, Writing - Original Draft, Visualization, Writing - Review & Editing.
Mohammad Reza Nikoo	Conceptualization, Methodology, Supervision, Writing - Review & Editing
Gholamreza Rakhshandehroo	Conceptualization, Methodology, Supervision, Writing - Review & Editing
Jan Franklin Adamowski	Supervision, Writing - Review & Editing
Amir Hossein Gandomi	Supervision, Writing - Review & Editing

REFERENCES

Aureli, F., Dazzi, S., Maranzoni, A., Mignosa, P., and Vacondio, R. 2015. "Experimental and numerical evaluation of the force due to the impact of a dam-break wave on a structure." *Advances in Water Resources*. https://doi.org/10.1016/j.advwatres.2014.11.009.

Barbosa, D. V. E., Santos, A. L. G., dos Santos, E. D., and Souza, J. A. 2019. "Overtopping device numerical study: Openfoam solution verification and evaluation of curved ramps performances." *International Journal of Heat and Mass Transfer*. https://doi.org/10.1016/j.ijheatmasstransfer.2018.11.071.

Bocchiola, D., Rulli, M. C., and Rosso, R. 2006. "Transport of large woody debris in the presence of obstacles."

Geomorphology. https://doi.org/10.1016/j.geomorph.2005.08.016.

Cheng, D., Zhao, X. zeng, Zhang, D. ke, and Chen, Y. 2017. "Numerical study of dam-break induced tsunami-like bore with a hump of different slopes." *China Ocean Engineering*. https://doi.org/10.1007/s13344-017-0078-2.

Crespo, A. J. C., Gómez-Gesteira, M., and Dalrymple, R. A. 2008. "Modeling dam-break behavior over a wet bed by a SPH technique." *Journal of Waterway, Port, Coastal and Ocean Engineering*. https://doi.org/10.1061/(ASCE)0733-950X(2008)134:6(313).

Dias, F., and Dutykh, D. 2007. "Dynamics of Tsunami waves." *NATO Security through Science Series C: Environmental Security*. https://doi.org/10.1007/978-1-4020-5656-7_8.

Duarte, R., Ribeiro, J., Boillat, J. L., and Schleiss, A. 2011. "Experimental Study on Dam-Break Waves for Silted-Up Reservoirs." *Journal of Hydraulic Engineering*. https://doi.org/10.1061/(ASCE)HY.1943-7900.0000444.

Evangelista, S., Altinakar, M. S., Di Cristo, C., and Leopardi, A. 2013. "Simulation of dam-break waves on movable beds using a multi-stage centered scheme." *International Journal of Sediment Research*. https://doi.org/10.1016/S1001-6279(13)60039-6.

Fluent Thoery Guide. 2013. "Ansys Fluent Theory Guide." *ANSYS Inc.,* USA, 15317(November), 724–746.

Fu, L., and Jin, Y. C. 2016. "mproved multiphase lagrangian method for simulating sediment transport in dam-break flows." *Journal of Hydraulic Engineering*. https://doi.org/10.1061/(ASCE)HY.1943-7900.0001132.

Gallegos, H. A., Schubert, J. E., and Sanders, B. F. 2009. "Two-dimensional, high-resolution modeling of urban dam-break flooding: A case study of Baldwin Hills, California." *Advances in Water Resources*. https://doi.org/10.1016/j.advwatres.2009.05.008.

Goseberg, N., Stolle, J., Nistor, I., and Shibayama, T. 2016. "Experimental analysis of debris motion due the obstruction from fixed obstacles in tsunami-like flow conditions." *Coastal Engineering*. https://doi.org/10.1016/j.coastaleng.2016.08.012.

Güney, M. S., Tayfur, G., Bombar, G., and Elci, S. 2014. "Distorted physical model to study sudden partial dam-break flows in an urban area." *Journal of Hydraulic Engineering*. https://doi.org/10.1061/(ASCE)HY.1943-7900.0000926.

Hänsch, S., Lucas, D., Höhne, T., and Krepper, E. 2014. "Application of a new concept for multi-scale interfacial structures to the dam-break case with an obstacle." *Nuclear Engineering and Design*. https://doi.org/10.1016/j.nucengdes.2014.02.006.

He, Z., Wu, T., Weng, H., Hu, P., and Wu, G. 2017. "Numerical simulation of dam-break flow and bed change considering the vegetation effects." *International Journal of Sediment Research*. https://doi.org/10.1016/j.ijsrc.2015.04.004.

Issakhov, A., and Imanberdiyeva, M. 2019. "Numerical simulation of the movement of water surface of dam-break flow by VOF methods for various obstacles." *International Journal of Heat and Mass Transfer*. https://doi.org/10.1016/j.ijheatmasstransfer.2019.03.034.

Issakhov, A., Zhandaulet, Y., and Nogaeva, A. 2018. "Numerical simulation of dam-break flow for various forms of the obstacle by VOF method." *International Journal of Multiphase Flow*. https://doi.org/10.1016/j.ijmultiphaseflow.2018.08.003.

Jeong, W., Yoon, J. S., and Cho, Y. S. 2012. “Numerical study on effects of building groups on dam-break flow in urban areas.” *Journal of Hydro-Environment Research*. https://doi.org/10.1016/j.jher.2012.01.001.

Kamra, M. M., Al Salami, J., Sueyoshi, M., and Hu, C. 2019. “Experimental study of the interaction of dambreak with a vertical cylinder.” *Journal of Fluids and Structures*. https://doi.org/10.1016/j.jfluidstructs.2019.01.015.

Kattel, P., Kafle, J., Fischer, J. T., Mergili, M., Tuladhar, B. M., and Pudasaini, S. P. 2018. “Interaction of two-phase debris flow with obstacles.” *Engineering Geology*. https://doi.org/10.1016/j.enggeo.2018.05.023.

Kocaman, S., and Ozmen-Cagatay, H. 2012. “The effect of lateral channel contraction on dam-break flows: Laboratory experiment.” *Journal of Hydrology*. https://doi.org/10.1016/j.jhydrol.2012.02.035.

LaRocque, L. A., Imran, J., and Chaudhry, M. H. 2013. “Experimental and numerical investigations of two-dimensional dam-break flows.” *Journal of Hydraulic Engineering*. https://doi.org/10.1061/(ASCE)HY.1943-7900.0000705.

Lauber, G., and Hager, W. H. 1998. “Experiments to dambreak wave: Horizontal channel.” *Journal of Hydraulic Research*. https://doi.org/10.1080/00221689809498620.

Mambretti, S., Larcan, E., and De Wrachien, D. 2008. “1D modelling of dam-break surges with floating debris.” *Biosystems Engineering*. https://doi.org/10.1016/j.biosystemseng.2008.02.011.

Miliani, S., Montessori, A., La Rocca, M., and Prestininzi, P. (2021). “Dam-Break Modeling: LBM as the Way towards Fully 3D, Large-Scale Applications.” *Journal of Hydraulic Engineering*, American Society of Civil Engineers (ASCE), 147(5).

Mokhtar, Z. A., Mohammed, T. A., Yusuf, B., and Lau, T. L. 2019. “Experimental investigation of tsunami bore impact pressure on a perforated seawall.” *Applied Ocean Research*. https://doi.org/10.1016/j.apor.2018.12.015.

Nilsson, H. 2010. “Proceedings of CFD with OpenSource Software.” Accessed September 2, 2021. http://dx.doi.org/10.17196/OS_CFD#YEAR_2010.

Open∇FOAM. 2015. “Open∇FOAM - The Open Source CFD Toolbox - User Guide.” *OpenFOAM Foundation 15th December 2015*.

Openfoamwiki. 2020. “Unofficial OpenFOAM wiki.” Accessed November 24, 2021. https://openfoamwiki.net/index.php/Main_Page.

Ozmen-Cagatay, H., and Kocaman, S. 2010. “Dam-break flows during initial stage using SWE and RANS approaches.” *Journal of Hydraulic Research*. https://doi.org/10.1080/00221686.2010.507342.

Ozmen-Cagatay, H., Kocaman, S., and Guzel, H. 2014. “Investigation of dam-break flood waves in a dry channel with a hump.” *Journal of Hydro-Environment Research*. https://doi.org/10.1016/j.jher.2014.01.005.

Panda, S. K., Singh, K. K., Shenoy, K. T., and Buwa, V. V. 2017. “Numerical simulations of liquid-liquid flow in a continuous gravity settler using OpenFOAM and experimental verification.” *Chemical Engineering Journal*. https://doi.org/10.1016/j.cej.2016.10.102.

Postacchini, M., Othman, I. K., Brocchini, M., and Baldock, T. E. 2014. “Sediment transport and morphodynamics generated by a dam-break swash uprush: Coupled vs uncoupled modeling.” *Coastal Engineering*. https://doi.org/10.1016/j.coastaleng.2014.04.003.

Saghi, H., and Lakzian, E. 2019. “Effects of using obstacles on the dam-break flow based on entropy generation analysis.” *European Physical Journal Plus*, Springer Verlag, 134(5). https://doi.org/10.1140/epjp/i2019-12592-3.

Schiller, L., and Naumann, Z. 1935. “A drag coefficient correlation.” *Z.Ver.Deutsch.Ing*, Elsevier Ltd, 77, 318-320. http://dx.doi.org/10.1016/j.ijheatmasstransfer.2009.02.006

Shi, H., Si, P., Dong, P., and Yu, X. 2019. “A two-phase SPH model for massive sediment motion in free surface flows.” *Advances in Water Resources*, Elsevier Ltd, 129, 80–98. https://doi.org/10.1016/j.advwatres.2019.05.006.

Singh, J., Altinakar, M. S., and Ding, Y. 2011. “Two-dimensional numerical modeling of dam-break flows over natural terrain using a central explicit scheme.” *Advances in Water Resources*. https://doi.org/10.1016/j.advwatres.2011.07.007.

Torres, C., Borman, D., Sleigh, A., and Neeve, D. (2021). “Application of Three-Dimensional CFD VOF to Characterize Free-Surface Flow over Trapezoidal Labyrinth Weir and Spillway.” *Journal of Hydraulic Engineering*, American Society of Civil Engineers (ASCE), 147(3), 04021002.

Valiani, A., Caleffi, V., and Zanni, A. 2002. “Case study: Malpasset dam-break simulation using a two-dimensional finite volume method.” *Journal of Hydraulic Engineering*. https://doi.org/10.1061/(ASCE)0733-9429(2002)128:5(460).

Vischer, D. L., and Hager, W. H. 1998. *Dam Hydraulics*. Wiley: Chichester, New York.

Vosoughi, F. 2018. “Experimental and Numerical Investigation of Dam-Break Phenomena in Silted-Up Reservoirs under Different Hydraulic Conditions.” M.Sc. thesis, Departement of civil and environmental engineering, Shiraz university, Shiraz, Iran.

[Dataset] Vosoughi, F., Nikoo, M. R., Rakhshandehroo, G., Adamowski, J. F. 2021a “Experimental dataset on sediment depths in scrutinizing the influences of downstream semi-circular obstacles on floods arising from the failure of dams with different levels of reservoir silting. V2.” Figshare. Dataset. Accessed November 24, 2021. https://doi.org/10.6084/m9.figshare.13686205

[Dataset] Vosoughi, F., Nikoo, M. R., Rakhshandehroo, G., Adamowski, J. F. 2021b “Experimental dataset on water levels in scrutinizing the influences of downstream semi-circular obstacles on floods arising from the failure of dams with different levels of reservoir silting. V2.” Figshare. Dataset. Accessed November 24, 2021. https://doi.org/10.6084/m9.figshare.13686142

[Dataset] Vosoughi, F., Nikoo, M. R., Rakhshandehroo, G., Adamowski, J. F. 2021c “Laboratory videos in scrutinizing the influences of downstream semi-circular obstacles on multi-layer shock waves with various sedimentation degrees in the upstream reservoir. V2.” Figshare. Media. Accessed November 24, 2021. https://doi.org/10.6084/m9.figshare.13677454

Wang, B., Liu, X., Zhang, J., Guo, Y., Chen, Y., Peng, Y., Liu, W., Yang, S., and Zhang, F. (2020a). “Analytical and Experimental Investigations of Dam-Break Flows in Triangular Channels with Wet-Bed Conditions.” *Journal of Hydraulic Engineering*, American Society of Civil Engineers (ASCE), 146(10), 04020070.

Wang, X., Chen, W., Zhou, Z., Zhu, Y., Wang, C., and Liu, Z. 2017. “Three-dimensional flood routing of a dam-break based on a high-precision digital model of a dense urban area.” *Natural Hazards*. https://doi.org/10.1007/s11069-016-2734-x.

Wang, Y., Liu, X., Yao, C., and Li, Y. (2020b). “Debris-Flow Impact on Piers with Different Cross-Sectional Shapes.” *Journal of Hydraulic Engineering*, American Society of Civil Engineers (ASCE), 146(1), 04019045.

Weller, H. G. 2008. “A New Approach to VOF-based Interface Capturing Methods for Incompressible and Compressible Flow.” *Technical Report,* (May), 13.

Wikipedia®. 2019. “Brumadinho dam disaster.” Accessed November 24, 2021. https://en.wikipedia.org/wiki/Brumadinho_dam_disaster.

Wu, W., and Wang, S. Y. 2007. “One-dimensional modeling of dam-break flow over movable beds.” *Journal of Hydraulic Engineering*. https://doi.org/10.1061/(ASCE)0733-9429(2007)133:1(48).

Xue, Y., Xu, W. L., Luo, S. J., Chen, H. Y., Li, N. W., and Xu, L. J. 2011. “Experimental study of dam-break flow in cascade reservoirs with steep bottom slope.” *Journal of Hydrodynamics*. https://doi.org/10.1016/S1001-6058(10)60140-0.

Yang, C. T. 1996. *Sediment transport : theory and practice*. *McGraw-Hill series in water resources and environmental engineering,* McGraw-Hill.

Zhang, M., and Wu, W. M. 2011. “A two dimensional hydrodynamic and sediment transport model for dam-break based on finite volume method with quadtree grid.” *Applied Ocean Research*. https://doi.org/10.1016/j.apor.2011.07.004.